

RUBIES: Evolved Stellar Populations with Extended Formation Histories at $z \sim 7-8$ in Candidate Massive Galaxies Identified with JWST/NIRSpec

BINGJIE WANG (王冰洁)^{1,2,3} JOEL LEJA^{1,2,3} ANNA DE GRAAFF⁴ GABRIEL B. BRAMMER^{5,6} ANDREA WEIBEL⁷
PIETER VAN DOKKUM⁸ JOSEPHINE F.W. BAGGEN⁸ KATHERINE A. SUESS^{9,*} JENNY E. GREENE¹⁰ RACHEL BEZANSON¹¹
NIKKO J. CLERI^{12,13} MICHAELA HIRSCHMANN¹⁴ IVO LABBÉ¹⁵ JORRYT MATTHEE¹⁶ IAN MCCONACHIE¹⁷
ROHAN P. NAIDU^{18,*} ERICA NELSON¹⁹ PASCAL A. OESCH^{7,5} DAVID J. SETTON^{10,†} AND CHRISTINA C. WILLIAMS^{20,21}

¹Department of Astronomy & Astrophysics, The Pennsylvania State University, University Park, PA 16802, USA

²Institute for Computational & Data Sciences, The Pennsylvania State University, University Park, PA 16802, USA

³Institute for Gravitation and the Cosmos, The Pennsylvania State University, University Park, PA 16802, USA

⁴Max-Planck-Institut für Astronomie, Königstuhl 17, D-69117, Heidelberg, Germany

⁵Cosmic Dawn Center (DAWN), Copenhagen, Denmark

⁶Niels Bohr Institute, University of Copenhagen, Jagtvej 128, Copenhagen, Denmark

⁷Department of Astronomy, University of Geneva, Chemin Pegasi 51, 1290 Versoix, Switzerland

⁸Department of Astronomy, Yale University, New Haven, CT 06511, USA

⁹Kavli Institute for Particle Astrophysics and Cosmology and Department of Physics, Stanford University, Stanford, CA 94305, USA

¹⁰Department of Astrophysical Sciences, Princeton University, Princeton, NJ 08544, USA

¹¹Department of Physics & Astronomy and PITT PACC, University of Pittsburgh, Pittsburgh, PA 15260, USA

¹²Department of Physics and Astronomy, Texas A&M University, College Station, TX, 77843-4242 USA

¹³George P. and Cynthia Woods Mitchell Institute for Fundamental Physics and Astronomy, Texas A&M University, College Station, TX, 77843-4242 USA

¹⁴Institute of Physics, Lab for Galaxy Evolution, EPFL, Observatoire de Sauverny, Chemin Pegasi 51, 1290 Versoix, Switzerland

¹⁵Centre for Astrophysics and Supercomputing, Swinburne University of Technology, Melbourne, VIC 3122, Australia

¹⁶Institute of Science and Technology Austria (ISTA), Am Campus 1, 3400 Klosterneuburg, Austria

¹⁷Department of Physics and Astronomy, University of California, Riverside, Riverside, CA 92521, USA

¹⁸MIT Kavli Institute for Astrophysics and Space Research, Cambridge, MA 02139, USA

¹⁹Department for Astrophysical and Planetary Science, University of Colorado, Boulder, CO 80309, USA

²⁰NSF's National Optical-Infrared Astronomy Research Laboratory, Tucson, AZ 85719, USA

²¹Steward Observatory, University of Arizona, Tucson, AZ 85721, USA

ABSTRACT

The identification of red, apparently massive galaxies at $z > 7$ in early James Webb Space Telescope (JWST) photometry suggests a strongly accelerated timeline compared to standard models of galaxy growth. A major uncertainty in the interpretation is whether the red colors are caused by evolved stellar populations, dust, or other effects such as emission lines or AGN. Here we show that three of the massive galaxy candidates at $z = 6.7-8.4$ have prominent Balmer breaks in JWST/NIRSpec spectroscopy from the RUBIES program. The Balmer breaks demonstrate unambiguously that stellar emission dominates at $\lambda_{\text{rest}} = 0.4 \mu\text{m}$, and require formation histories extending hundreds of Myr into the past in galaxies only 600–800 Myr after the Big Bang. Two of the three galaxies also show broad Balmer lines, with $\text{H}\beta$ FWHM $> 2500 \text{ km s}^{-1}$, suggesting that dust-reddened AGN contribute to, or even dominate, the SEDs of these galaxies at $\lambda_{\text{rest}} \gtrsim 0.6 \mu\text{m}$. All three galaxies have relatively narrow [O III] lines, seemingly ruling out a high-mass interpretation if the lines arise in dynamically-relaxed, inclined disks. Yet, the inferred masses also remain highly uncertain. We model the high-quality spectra using Prospector to decompose the continuum into stellar and AGN components, and explore limiting cases in stellar/AGN contribution. This produces a wide range of possible stellar masses, spanning $M_{\star} \sim 10^9 - 10^{11} M_{\odot}$. Nevertheless, all fits suggest a very early and rapid formation, most of which follow with a truncation in star formation. Potential origins and evolutionary tracks for these

objects are discussed, from the cores of massive galaxies to low-mass galaxies with over-massive black holes. Intriguingly, we find all of these explanations to be incomplete; deeper and redder data are needed to understand the physics of these systems.

Keywords: Active galactic nuclei (16) – AGN host galaxies (2017) – Galaxy evolution (594) – Galaxy formation (595) – High-redshift galaxies (734) – Spectral energy distribution (2129)

1. INTRODUCTION

In the cores of the most massive galaxies in the local universe, stars have inferred stellar age of ~ 13 Gyr and high α -element abundance, suggesting their stellar components are formed at $z \gtrsim 5$ in a spectacular and short burst of star formation (e.g., [Thomas et al. 2005](#)). This hypothesis was bolstered by the discovery of their putative $z \sim 2$ progenitors, compact galaxies with high stellar masses $\sim 10^{11} M_\odot$ and small effective radii of ~ 1 kpc, which importantly have stellar densities similar to the cores of $z \sim 0$ ellipticals ([Bezanson et al. 2009](#)). When exactly their stellar bodies formed, however, has not yet been clearly established. While some likely compact star-forming progenitors have been identified at $z = 2 - 3$ ([Nelson et al. 2014](#); [Barro et al. 2014](#)), simulations and number density arguments suggest that at least some of these massive cores must have formed earlier ([Wellons et al. 2015](#)). This has since been buttressed by the James Webb Space Telescope (JWST) discovering and characterizing massive quiescent galaxies at $z = 2 - 5$, with stellar bodies of $10^{10.5-11} M_\odot$ and inferred formation redshifts of $z \gtrsim 7$ ([Carnall et al. 2023](#); [Glazebrook et al. 2024](#); [de Graaff et al. 2024a](#); [Park et al. 2024](#)). Taken at face value, this implies a very rapid formation and quenching of very massive galaxies in the first billion years of the universe—a spectacular event that should produce a huge amount of observable light. Yet, while candidates have been found (e.g., [Hashimoto et al. 2018](#); [Williams et al. 2023](#)), the progenitors of these quenched galaxies existing at $t_{\text{univ}} \sim 1$ Gyr have yet to be conclusively identified.

Contemporaneously, one of the most surprising early discoveries made with the JWST is the identification of a population of seemingly massive ($M_\star \gtrsim 10^{10} M_\odot$), compact (effective radii $\lesssim 1$ kpc), and rest-optical red galaxies at redshift $z > 6$ via a double-break color selection ([Labbé et al. 2023a](#); hereafter L23). This selection targets distinct spectral energy distributions (SEDs) which include a drop-out at $\sim 1 \mu\text{m}$ and a very red color at $\sim 3 \mu\text{m}$. This is a highly efficient selection for $7 \lesssim z \lesssim 9$

objects, but the red rest-frame optical color may be driven by very different underlying physics: it could come from a Balmer break, from strong emission lines, from a very red continuum, or from some combination of these features.

In their main analysis, [Labbé et al. \(2023a\)](#) interpreted the red color as a combination of Balmer break and a very red rest-optical stellar continuum. This interpretation yields very high stellar mass-to-light ratio (M/L) and implies extreme stellar masses, up to $M_\star \sim 10^{11} M_\odot$. While massive galaxies must form early and quickly, this would imply that these objects both emerged earlier and hosted more mass than expected. Indeed, it soon became clear that such early massive galaxies are difficult to make in the standard model of cosmology, as the amount of baryons inferred in stars is comparable to the cosmic baryon abundance in these early halos ([Boylan-Kolchin 2023](#)). Star formation feedback processes typically limit the fraction of baryons locked up in stars to far below the cosmic baryon fraction.

These uncomfortably high stellar masses prompted a wave of alternative explanations for the observed fluxes and colors, including extreme emission line galaxies ([Endsley et al. 2023](#)), a top-heavy stellar initial mass function ([Boylan-Kolchin 2023](#); [Steinhardt et al. 2023](#)), or obscured active galactic nuclei (AGN) ([Kocevski et al. 2023](#); [Barro et al. 2024](#)). Obscured AGNs significantly lower the inferred stellar masses by contributing to the red optical continuum flux. They can also lower the photometric redshift, and so decrease the inferred number densities of massive galaxies at high redshifts. In addition to their red color, the L23 sample exhibits compact morphology, supporting the idea that AGN could contribute to the fluxes.

Indeed, one of the bright red objects in L23 has been confirmed to host a broad-line AGN at a lower redshift of $z = 5.62$ ([Kocevski et al. 2023](#)), and the more broadly defined red compact sources (often dubbed as little red dots, or LRDs; e.g., [Labbé et al. 2023b](#); [Matthee et al. 2024](#)) have shown a prevalence of broad-line AGNs ([Greene et al. 2024](#)). However, as shown in [Baggen et al. \(2023\)](#), most of the L23 sample are marginally resolved at rest-UV wavelengths—so their rest-UV flux at least

* NHFP Hubble Fellow

† Brinson Prize Fellow

is not dominated by a point source. Furthermore, the inferred densities, assuming that the L23 objects are galaxies, are consistent with the central regions of today’s elliptical galaxies.

Therefore, these objects may still be massive galaxies with evolved populations at high redshifts—in fact, it would be surprising if star formation slowed sufficiently to show prominent Balmer breaks at high redshift without influence from an AGN. The two massive quiescent systems currently known at $z \sim 5$ both show indications of AGN activity (Carnall et al. 2023; de Graaff et al. 2024a). It has long been suspected that the stellar cores of galaxies must have co-formed with their supermassive black holes; such a formation scenario is the simplest interpretation of the observed tight correlation between the mass of the bulge and the mass of the central supermassive black hole (Ferrarese & Merritt 2000). The key questions regarding these red objects are therefore threefold: (i) are the photometric redshifts accurate; or more generally, what is the source of the red colors—emission lines, continua, or spectral breaks? (ii) do these objects host evolved stellar populations? and (iii) how much of the continuum is powered by stellar versus AGN emission? These core questions are unanswerable without rest-frame optical spectra.

Here we conduct a follow-up study on double-break candidates selected from the RUBIES JWST/NIRSpec spectroscopic program (JWST-GO-4233; PIs de Graaff & Brammer). These targets partially overlap with the L23 sample, and were observed with high priority for their red colors ($F150W - F444W > 2$), and bright apparent magnitudes ($F444W < 26$ mag). In this paper, we present three objects with detected Balmer breaks, existing as early as $z_{\text{spec}} = 8.35$, suggesting a formation history extending hundreds of Myr into the past of the galaxies observed only 600–800 Myr after the Big Bang. Unambiguous broad emission lines are also observed in 2/3 objects, motivating a deeper look at the source of the red continua.

The structure of this paper is as follows. Section 2 provides an overview of the data. Section 3 presents the key observational features of these objects, including observed Balmer breaks and broad lines. Section 4 focuses on the analysis of the emission lines, while Section 5 details the AGN and host galaxy composite SED modeling. Section 6 presents evidence for/against the different proposed physical models, including kinematics, formation histories, and population-level characteristics. We conclude in Section 7 with discussion of possible interpretations and evolutionary scenarios, and outstanding questions.

Where applicable, we adopt the best-fit cosmological parameters from the WMAP 9 yr results: $H_0 = 69.32$ $\text{km s}^{-1} \text{Mpc}^{-1}$, $\Omega_M = 0.2865$, and $\Omega_\Lambda = 0.7135$ (Hinshaw et al. 2013). Unless otherwise mentioned, we assume the Chabrier initial mass function (Chabrier 2003), and report the median of the posterior, with associated 1σ error bars being the 16th and 84th percentiles.

2. DATA

The spectroscopic survey RUBIES uses JWST/NIRSpec to observe approximately 4000–5000 sources selected from public NIRCам imaging in the UDS and EGS fields. It utilizes the NIRSpec microshutter array (MSA; Ferruit et al. 2022) with both the low-resolution Prism/CLEAR and medium-resolution G395M/F290LP disperser/filter combinations. The sample in this paper was targeted in 6 masks observed in March 2024. Figure 1 presents an overview of the sample in color space.

Reduction of the imaging data is presented in Valentino et al. (2023) while the spectroscopic reductions are described in Heintz et al. (2024); Wang et al. (2024a). Full details of the RUBIES observing program and data reduction will be detailed in de Graaff et al. in prep. The subsequent sections provide a brief summary.

2.1. Imaging

The RUBIES targets in the EGS were selected from public JWST/NIRCам data from the Cosmic Evolution Early Release Science Survey (CEERS, JWST-GO-1345; PI Finkelstein; Bagley et al. 2023; Finkelstein et al. 2023), which provides imaging in 7 bands (F115W, F150W, F200W, F277W, F356W, F410M, and F444W). Additionally, we use archival imaging in 7 different filters (F435W, F606W, F814W, F105W, F125W, F140W, and F160W) from the Hubble Space Telescope (HST) from the CANDELS survey (Grogin et al. 2011; Koekemoer et al. 2011).

The image mosaics, with a pixel scale of $0.04'' \text{pix}^{-1}$, are publicly available in the DAWN JWST Archive (DJA; version 7.2) and were reduced using *grizli* (Brammer 2023a). Fluxes are measured from PSF-matched images in circular apertures with a radius of $0.16''$, and then Kron-corrected to the total flux, as described in Weibel et al. (2024).

2.2. Spectroscopy and Sample Selection

Each target was observed for 48 min in the Prism/Clear mode and the G395M/F290LP mode, using a standard 3-shutter slitlet and 3-point nodding pattern. The spectra are reduced, combined and extracted using *msaexp* (Brammer 2023b). To account for wavelength-dependent flux calibration that is not yet captured well

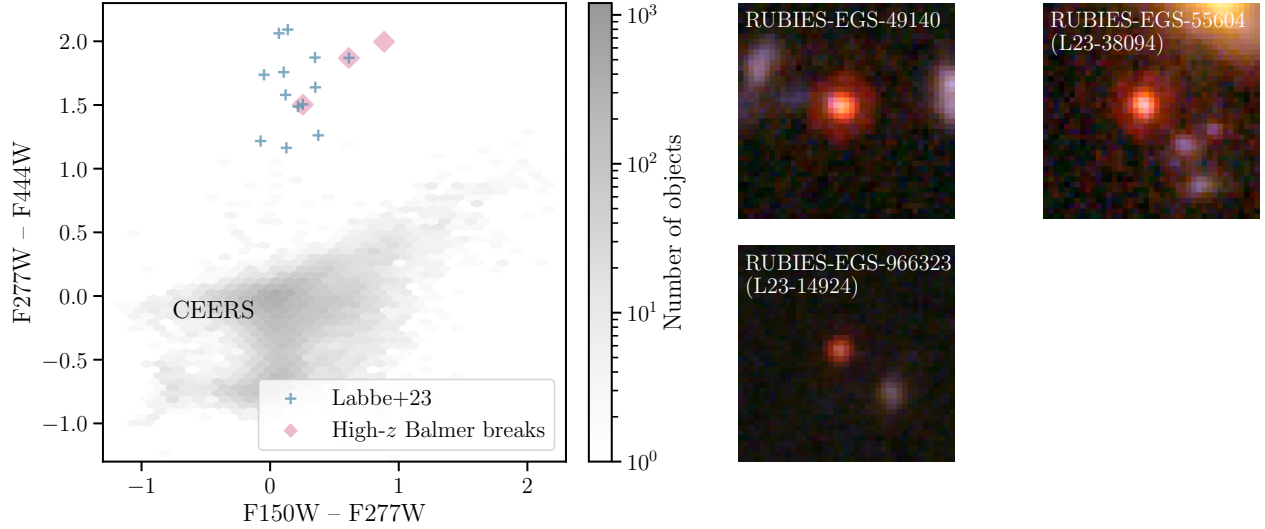


Figure 1. Sample of this paper. (Left) This work focuses on continuum-detected sources with Balmer breaks, shown as solid diamonds on the color plane. The L23 sample is denoted as plus signs, and all sources in CEERS brighter than 27 AB mag are grey hexagons included for reference. (Right) We show the $2 \times 2''$ color images of the three Balmer-break-detected sources, colors from JWST/NIRCam F115W, F277W, and F444W. They are remarkably compact at red wavelengths, with some evidence for spatial structure at blue wavelengths.

by the pipeline, we re-normalize the Prism spectrum to match the NIRCam photometry using a dynamic high-order polynomial as described in Section 5. The G395M spectrum is subsequently rescaled by this polynomial. We find that there is a small systematic offset ($\approx 10 - 20\%$) in the flux calibration between the Prism and G395M spectra, which has recently also been reported by D’Eugenio et al. (2024). To determine the offset we fit the [O III] doublet in both the Prism and G395M spectra (§ 4), and hence rescale the full G395M spectrum by the ratio of the two to match the flux calibration of the Prism spectrum.

This paper focuses on the 3 targets in this sample that exhibit clear Balmer breaks at $z_{\text{spec}} = 6.6 - 8.4$, found via visual inspection of the 2D and 1D spectra. These objects are extremely red in F277W – F444W (Figure 1), the characterization of red objects being one of the core targeting criteria of RUBIES. In what follows, we establish the detections of Balmer breaks, and the broad emission lines, which are the two key characteristics of this sample.

3. THE COEXISTENCE OF BALMER BREAKS AND BROAD EMISSION LINES AT $z = 6.6 - 8.4$

The most striking discovery is the seeming appearance of Balmer breaks observed between $z = 6.7 - 8.4$. These are produced in the atmospheres of older stars and typically only appear in evolved stellar populations after a significant reduction in star formation rate (SFR) last-

ing at least ~ 100 Myr (Bruzual A. 1983; Hamilton 1985; Worthey et al. 1994; Balogh et al. 1999). It is surprising to see SEDs dominated by evolved stellar populations at these times—the age of the universe for the highest redshift object ($z = 8.35$) is 610 Myr, giving very little time to form the stellar populations. This suggests an extremely rapid and early formation for these objects. The highest redshift candidate at $z = 8.35$ represents the highest-redshift Balmer break identified to date, with the next-highest redshift being a $z = 7.3$ object with a low mass of $10^{8.5} M_{\odot}$ (Looser et al. 2023).

To verify that the observed spectral breaks are indeed Balmer breaks, as opposed to observational artifacts or a mis-identification of spectral breaks driven by other physics, we take the average of the three observed spectra after scaling each spectrum by the median of the continuum flux close to the break (between 4150 and 4250 Å in rest frame). The same average is then calculated for the best-fit galaxy model spectra (§ 5). We show the normalized individual Prism spectra, over-plotted with the averaged model spectra in Figure 2. It is evident that all the breaks are located at the expected wavelength, and have similar shapes, buttressing the Balmer break interpretation. Critically, the stacked galaxy model spectra agree well with the data, suggesting that the model fits are also properly interpreting the light as evolved stellar populations. Section 5 elaborates on the SED modeling.

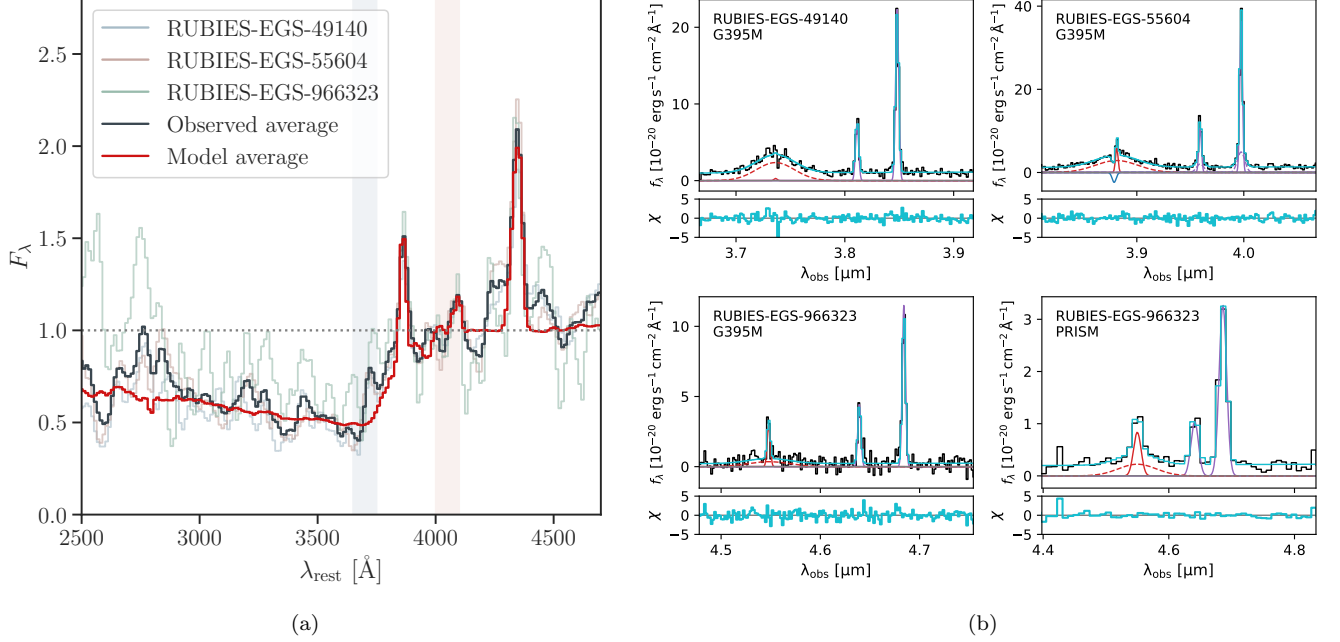


Figure 2. Characteristics of the sample of this paper. (a) Balmer breaks detected at $z_{\text{spec}} = 6.7 - 8.4$. The scaled individual spectra which exhibit potential Balmer breaks are plotted in light colors, and the averaged spectrum is shown in black. Overplotted in red is the averaged best-fit model spectrum (§5). All breaks are located at the expected wavelength, and show similar shapes, supporting the Balmer break interpretation. The break strength for the average observed spectrum, quantified by the flux ratio in the wavelength windows illustrated in blue and red shades, is 1.71. (b) Emission line fits to the $H\beta$ and $[O\text{ III}]$ complex (§4). We find unambiguous broadened $H\beta$ lines in the G395M spectrum for two sources (RUBIES-EGS-49140 and 55604), indicative of an AGN. We show both the G395M and Prism fits for RUBIES-EGS-966323, for which the broad component of $H\beta$ is only marginally detected.

A commonly used measure of the Balmer break strength is D_{4000} , as originally defined in Bruzual A. (1983); Balogh et al. (1999). However, the wavelength windows in these definitions locate redward of the Balmer limit (3645 Å) and overlap with the $[O\text{ II}]$ emission line. While Binggeli et al. (2019) proposed a new definition using the fluxes in $[3400, 3600]$ Å and $[4150, 4250]$ Å, the larger separation means that this definition is more sensitive to the overall slope of the spectrum. Therefore, we determine the break strength using two windows at $[3650, 3750]$ Å and $[4000, 4100]$ Å instead, which can still be compared fairly to other Balmer break measurements. These windows avoid contamination from strong nebular line emission and are close enough to be minimally impacted by dust attenuation, or the overall slope of the spectrum. The break strengths for RUBIES-EGS-49140, 55604, and 966323 are 2.07 ± 0.06 , 1.76 ± 0.06 , and 1.35 ± 0.11 , respectively.

In addition to hosting Balmer breaks, we note that the broad emission lines are evident in the spectra of RUBIES-EGS-49140 and 55604, as shown in Figure 2, while the existence of broad $H\beta$ is more ambiguous for the final object RUBIES-EGS-966323. These observations motivate detailed emission line fitting to decom-

pose them into broad and (potentially) narrow components, and also present an opportunity to estimate black hole masses. We do so in Section 4.

4. EMISSION LINES

4.1. Emission Line Decomposition

We use the G395M spectra to model the emission line widths of the Balmer $H\beta$ and $[O\text{ III}]$ lines. Prior to fitting we rescale the error spectrum, as we find that the noise estimated by the `msaexp` pipeline is underestimated compared to the observed pixel-to-pixel variation. To estimate the rescaling factor we select the region outside of the $H\beta$ and $[O\text{ III}]$ emission lines and calculate the ratio between the pixel-to-pixel variance and the median of the error spectrum; this results in a rescaling factor in the range 1.3 – 2.0.

Our fitting methodology broadly follows that described in Wang et al. (2024a): given the compact morphology of the sources (Baggen et al. 2023), we use a point source line-spread function (LSF) from de Graaff et al. (2024b) and the Markov Chain Monte Carlo (MCMC) ensemble sampler `emcee` (Foreman-Mackey et al. 2013) to estimate the posteriors. Crucially, our method explicitly includes a systematic uncertainty on

the model LSF, and therefore provides realistic measurement uncertainties for marginally-resolved lines.

We select the region around the emission line complex ($\pm 0.2 \mu\text{m}$), and begin by masking the $\text{H}\beta$ line (a region of 7000 km s^{-1}) to fit only the $[\text{O III}]$ doublet to estimate the narrow line width and redshift of the source. We use a single Gaussian component, the dispersion of which is the same for both lines of the $[\text{O III}]$ doublet and constrained to be in the range $\sigma_{\text{narrow}} \in [0, 500] \text{ km s}^{-1}$ using a uniform prior. The continuum is fit with a 1st order polynomial. We then explore whether the $[\text{O III}]$ lines show evidence for a second broader component by fitting a 2-component Gaussian model, where the width of the second Gaussian is constrained to be larger than that of narrow component. We compute the Bayesian information criterion (BIC) to compare the two models (Jeffreys 1961; Liddle 2004). We find evidence ($\Delta\text{BIC} = 13$) for a broader component in the $[\text{O III}]$ line for RUBIES-EGS-55604 with a dispersion $\sigma_{\text{broad}, \text{OIII}} = 248^{+61}_{-41} \text{ km s}^{-1}$, and no evidence for a second component in the other two sources.

Next, we include the $\text{H}\beta$ line in the fitting. We first fit a single Gaussian component for the $\text{H}\beta$ line. Given the limited S/N of the data, we tie the width of this component to that of the $[\text{O III}]$ lines. We then include a second broad component for the $\text{H}\beta$ line, where $\sigma_{\text{broad}} \in [500, 2500] \text{ km s}^{-1}$. For RUBIES-EGS-55604 we find a blue-shifted absorption feature in the $\text{H}\beta$ line, which we model as an additional Gaussian component with a velocity offset $\Delta v \in [0, 1000] \text{ km s}^{-1}$ and dispersion $\sigma_{\text{outflow}} \in [0, 1000] \text{ km s}^{-1}$. Such absorption feature in Balmer and/or He lines has been seen in recent studies of AGNs as well (Kocevski et al. 2024; Matthee et al. 2024; Wang et al. 2024a). The multi-component fits and the residuals are shown in Figure 2.

Again, using the BIC to compare the models, we find that RUBIES-EGS-49140 and 55604 have unambiguous broad components in the $\text{H}\beta$ line ($\Delta\text{BIC} > 100$). The third source, RUBIES-EGS-966323, is fainter and at higher redshift, and has only a marginal detection of a broad component ($\Delta\text{BIC} = 1.94$; broad line flux detected at 3.5σ , $F_{\text{H}\beta, \text{broad}} = 2.1 \pm 0.6 \times 10^{-18} \text{ erg s}^{-1} \text{ cm}^{-2}$). For this source we also perform an independent fit of the Prism spectrum, finding similarly weak evidence for a two-component model and posteriors that are consistent with the fit to the G395M spectrum.

Finally, we also fit the Balmer $\text{H}\alpha$ emission line, which is available in the G395M spectrum for RUBIES-EGS-49140 and only in the Prism spectrum for RUBIES-EGS-55604 (for RUBIES-EGS-966323 $\text{H}\alpha$ is red-shifted out of the wavelength range accessible with NIRSpect).

We use both a narrow and broad component for $\text{H}\alpha$, and also model the $[\text{N II}]_{\lambda\lambda 6549, 6585}$ doublet. We assume that $[\text{N II}]$ is narrow and set the width to be equal to that of the narrow $\text{H}\alpha$ line, and fix the flux ratio of the doublet to 1:2.94. Moreover, informed by the fits to $\text{H}\beta$ and $[\text{O III}]$, we constrain the dispersion of the narrow lines to $< 150 \text{ km s}^{-1}$. For RUBIES-EGS-49140 we also find a blue-shifted absorption feature in the $\text{H}\alpha$ line, which we fit in the same manner as described previously for the $\text{H}\beta$ line of RUBIES-EGS-55604. We note that we use these fits only to obtain an estimate of the broad line flux in order to calculate the broad $\text{H}\alpha$ equivalent width in Section 6.1.

4.2. Single-epoch Black Hole Mass Estimates

Reverberation mapping is a method employed to determine the size of the broad-line region by analyzing the time delay between variations in the AGN continuum and corresponding changes in the broad permitted lines (e.g., Blandford & McKee 1982). It has enabled the establishment of empirical correlations between the size, line luminosities, and widths in the nearby universe (e.g., Kaspi et al. 2000; Landt et al. 2013). These correlations facilitate the estimation of black hole masses from single-epoch observations.

We estimate the black hole mass based on $\text{H}\beta$ and luminosity at rest 5100 \AA , following Assef et al. (2011):

$$\log(M_{\text{BH}}/M_{\odot}) = 0.895 + 0.529 \log \left(\frac{L_{5100}}{10^{44} \text{ erg s}^{-1}} \right) + 2.0 \log \left(\frac{\text{FWHM}_{\text{H}\beta}}{\text{km s}^{-1}} \right). \quad (1)$$

$\text{H}\beta$ is used since $\text{H}\alpha$ is not available for all sources and suffers from uncertainty due the blending of the $[\text{N II}]$ doublet with the broad component of $\text{H}\alpha$. L_{5100} is calculated from the intrinsic AGN spectrum inferred from the SED models. We adopt this relation to better illustrate the uncertain in the black masses, as the different SED models predict a wide range of AGN luminosities. All line luminosities here are dereddened using the dust attenuation inferred from SED fitting. While subject to systematic uncertainties, this represents our best estimate of the dust content in the absence of a Balmer decrement.

We note, however, that additional systematic uncertainties are likely introduced by the application of these methods at higher redshifts and in different physical conditions than where they are calibrated (e.g., Yue et al. 2024).

5. SPECTRAL ENERGY DISTRIBUTION MODELING

The clear detection of the Balmer breaks means that the rest-frame 3500 Å wavelength range is dominated by starlight. However, Balmer breaks are indicative only that evolved stellar populations exist and are relatively bright—they can appear even with ongoing star formation. Therefore, unambiguous Balmer breaks leave some room for interpretation when inferring formation histories. The mixture of stellar (as suggested by the Balmer break) and AGN continuum emission (as suggested by the broad emission lines) motivate the need for detailed spectrophotometric modeling which includes contributions from both components.

Given that decomposing galaxy/AGN light is a known challenge, we consider three models to capture the systematic uncertainties in the inferred properties and formation histories. Below we describe the free and fixed parameters of the SED model, and then introduce three different priors which lead to three different interpretations of the observed light.

5.1. Core Model Components

The available JWST and HST photometric data are jointly fitted with the full NIRSpec/Prism spectrum within the **Prospector** inference framework (Johnson et al. 2021), following Wang et al. (2024a). The setup for the stellar populations is detailed in Wang et al. (2024b). In brief, we adopt the MIST stellar isochrones (Choi et al. 2016; Dotter 2016) along with the MILES stellar spectral library (Sánchez-Blázquez et al. 2006) in FSPS (Conroy & Gunn 2010). Star formation history (SFH) follows the non-parametric **Prospector- α** description, characterizing mass formation in 7 logarithmically-spaced time bins (Leja et al. 2017), with a weakly informative prior assumption of a rising SFH from Wang et al. (2023). Dust attenuation is described by a Calzetti et al. (2000) curve with a flexible power-law slope (Noll et al. 2009). The fraction of starlight permitted outside the dust screen is allowed to vary, a non-zero fraction of which suggests the presence of blue stars possibly existing outside the dust or having created holes within it. Dust emission is incorporated based on the model by Draine & Li (2007).

Model spectra are convolved with the NIRSpec/Prism instrumental resolution curve, tailored for a point source morphology using **msafit** (de Graaff et al. 2024b). We account for wavelength-dependent slit losses by scaling the normalization of the spectrum to match the photometry through a 7th-order polynomial calibration vector applied during the fitting process.

Emission lines are fit using a one-component Gaussian model, and where applicable, a two-component Gaussian model to account for the narrow and broad com-

ponents. This approach means that the emission lines are not interpreted physically, merely described and included in the modeling of the photometry. To prevent the likelihood from being influenced by residuals from non-Gaussian line kinematics, we enforce a 10% error floor in the spectroscopic data, which is higher than the conventional 5% error floor applied to photometry. However, we introduce a multiplicative noise inflation term, with a prior range from 0.5 to 5. Typically, this value is found to be around 1.5, suggesting an additional 50% inflation of the random noise produces a good fit. The posteriors are sampled via the dynamic nested sampler **dynesty** (Speagle 2020).

5.2. Continuum Contribution from A Dusty Active Galactic Nucleus

The composite galaxy and AGN model is presented in Wang et al. (2024a), in which we approximate the direct ultraviolet (UV)–optical emission from an AGN accretion disk as piece-wise power laws, with varying normalization. The slopes are fixed to the best-fit values in Temple et al. (2021), which are calibrated to the median colors of quasars in SDSS, UKIDSS, and unWISE. The light from the accretion disk experiences the same dust attenuation as the stars, but is additionally reddened by a separate dust attenuation curve modeled as a power law with varying normalization and shape. In all, the AGN continuum is controlled by 5 free parameters (the AGN-to-galaxy flux ratio, and four dust attenuation parameters, two of which are shared with the galaxy light).

5.3. Modeling A Range of Possible Stellar and AGN Contribution to the Rest-optical Continua

The key uncertainty in the interpretation of these objects is the source of the red continuum: is it powered by AGN, stars, or a mixture of both? The implied total stellar masses and formation histories are a strong function of this decomposition. A very red, luminous rest-frame optical stellar solution has a high M/L and an extended formation history, whereas a blue and/or less luminous stellar optical continuum can instead be fit with a flat or rising SFH and relatively little stellar mass. The Balmer break is a key constraint here as this, alongside the resolved sizes in the blue (Baggen et al. 2023), suggest the continuum bluewards of rest-4000 Å is dominated by stars.

The central question is therefore the origin of the continuum redward of the Balmer break. We consider three models which bracket the possible range of inferred stellar and AGN contribution to the observed rest-optical continua.

5.3.1. Maximal Stellar Contribution

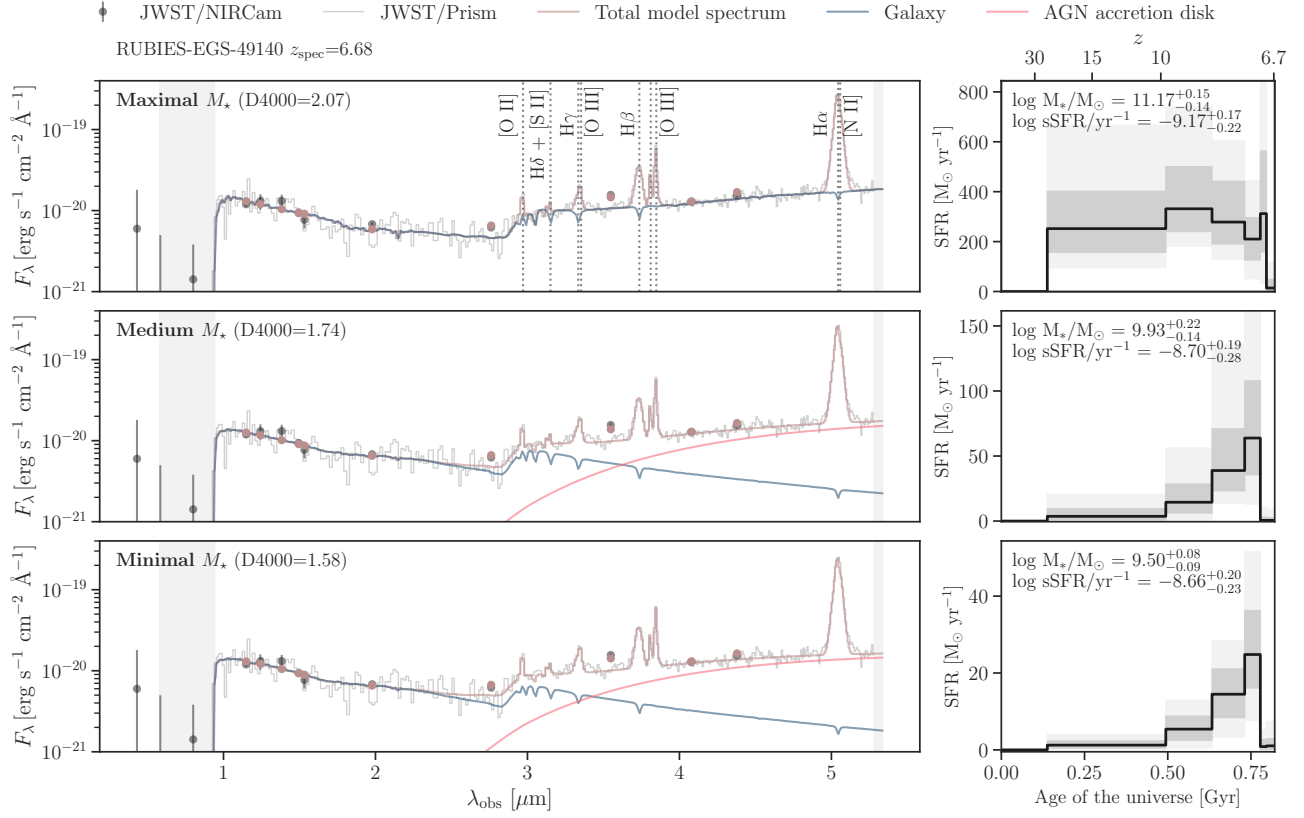


Figure 3-a. Spectrophotometric modeling for RUBIES-EGS-49140, with models including maximal / medium / minimal stellar contribution shown. The other two objects with detected Balmer breaks are shown in subsequent figures. (Left panels) The photometric and spectroscopic data are shown in gray. The best-fit model spectrum, which includes the marginalized emission lines as annotated, is plotted in light brown. The galaxy and the AGN continuum components are over-plotted in blue and red, respectively. The break strength, D4000, predicted by the galaxy model spectrum is indicated to the upper left corner. The spectral regions that are masked due to low S/N or detector gap are shaded in gray. (Right panels) The inferred SFRs are plotted as a function of the age of the universe. The gray and light gray shading indicates 1σ and 2σ uncertainties, respectively. The post-starburst feature is primarily driven by the Balmer break.

We begin by considering a model which maximizes the stellar contributions. This is achieved by placing a log-normal prior on the pre-dust-attenuated AGN-to-galaxy flux ratio at rest 5500 Å, $f_{\text{AGN},5500\text{\AA}}$, with mean $\mu = -3$, and standard deviation $\sigma = 1$. A log-uniform (i.e., flat in log-space) prior is used on the galaxy mass.

This model down-weights the AGN contribution at wavelengths where it is naturally brightest, and effectively leads to stellar masses similar to those from a “galaxy-only” fit. While this serves as a useful benchmark, it also implies the broad line equivalent widths (EWs), assuming they are driven by AGN, are extremely, perhaps unphysically, high.

5.3.2. A Mixture of AGN and Stellar Contributions

We also define a middle ground model, where log-uniform priors are assumed on the total mass formed

and $f_{\text{AGN},5500\text{\AA}}$. While it is impossible to write down an agnostic prior, the intent here is to let the data inform the inference process to the maximal extent. This model typically falls between the “maximum” and “minimum” stellar contributions. However, this does not mean that this model is to be taken as the fiducial model or in some way better motivated than the other choices. The available spectroscopic data are not constraining enough to break the degeneracies among the stellar populations, black hole properties, and dust attenuation.

5.3.3. Minimal Stellar Contribution

For the minimal stellar model, we impose a prior on the galaxy mass, with the probability $P(M) \propto M^\alpha$. The slope, $\alpha = -1.7$, is taken to be the low-mass slope of the theoretical stellar mass function at $z = 7$ (Tacchella et al. 2018). This prior is not intended to exactly

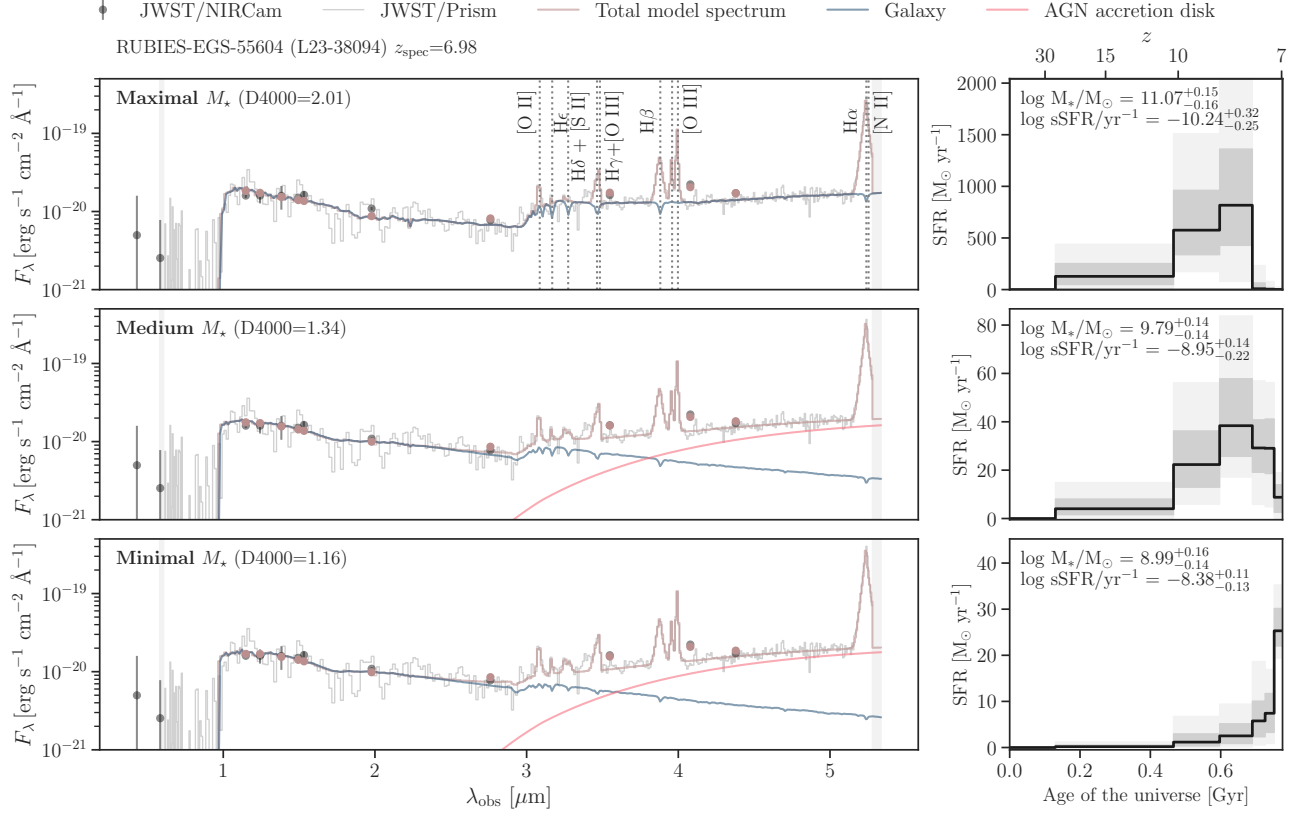


Figure 3-b. Spectrophotometric modeling for RUBIES-EGS-55604 (identified as 38094 in L23), with format as described in Figure 3-a.

replicate the mass function and serves its purpose of producing a low-mass solution even if the true mass function has a different low-mass slope.

A more intuitive prior down-weighting the galaxy contribution would be on the fractional light contribution instead of directly on the stellar mass, as is done with the maximal stellar model. However, the complex translation from light to mass means that, with a prior on the light only, the dust and stellar M/L can adjust to keep the stellar masses similar; a direct prior on the stellar mass avoids this degeneracy.

6. RESULTS

Here we describe the properties resulting from the individual fits to the three objects with Balmer breaks detected at $z_{\text{spec}} = 6.7 - 8.4$. As alluded to in Section 5, even in the presence of an unambiguous Balmer break, there can be a wide range of inferred star formation histories. The Balmer break strengths, as measured using our definition of D4000 in Section 3, vary from 2.1 to 1.6 (Figure 3-a), 2.0 to 1.2 (Figure 3-b), and 1.7 to 1.1

(Figure 3-c), by altering the AGN contribution from ~ 0 to $\sim 100\%$ for RUBIES-EGS-49140, 55604, and 966323, respectively.

The range of D4000 also suggests that the adopted sets of SED models bracket the uncertainty in continuum decomposition. As summarized in Table 1, the medium stellar model typically leads to $M_* \sim 10^{9.8} M_\odot$. If the red optical light is instead driven by an older dusty stellar population, M/L can rise dramatically, producing masses up to $M_* \sim 10^{11} M_\odot$. In the other direction, a prior that minimizes the inferred stellar masses can still reproduce the light while lowering the inferred masses by up to 1 dex.

In this section we lay out the physical properties and the implications of the formation histories inferred by the three physical models, including both observational and evolutionary considerations. The aim here is to provide an unbiased, comprehensive view into the very different possible physical interpretations of these objects—all of which result in statistically acceptable fits to the observed spectra.

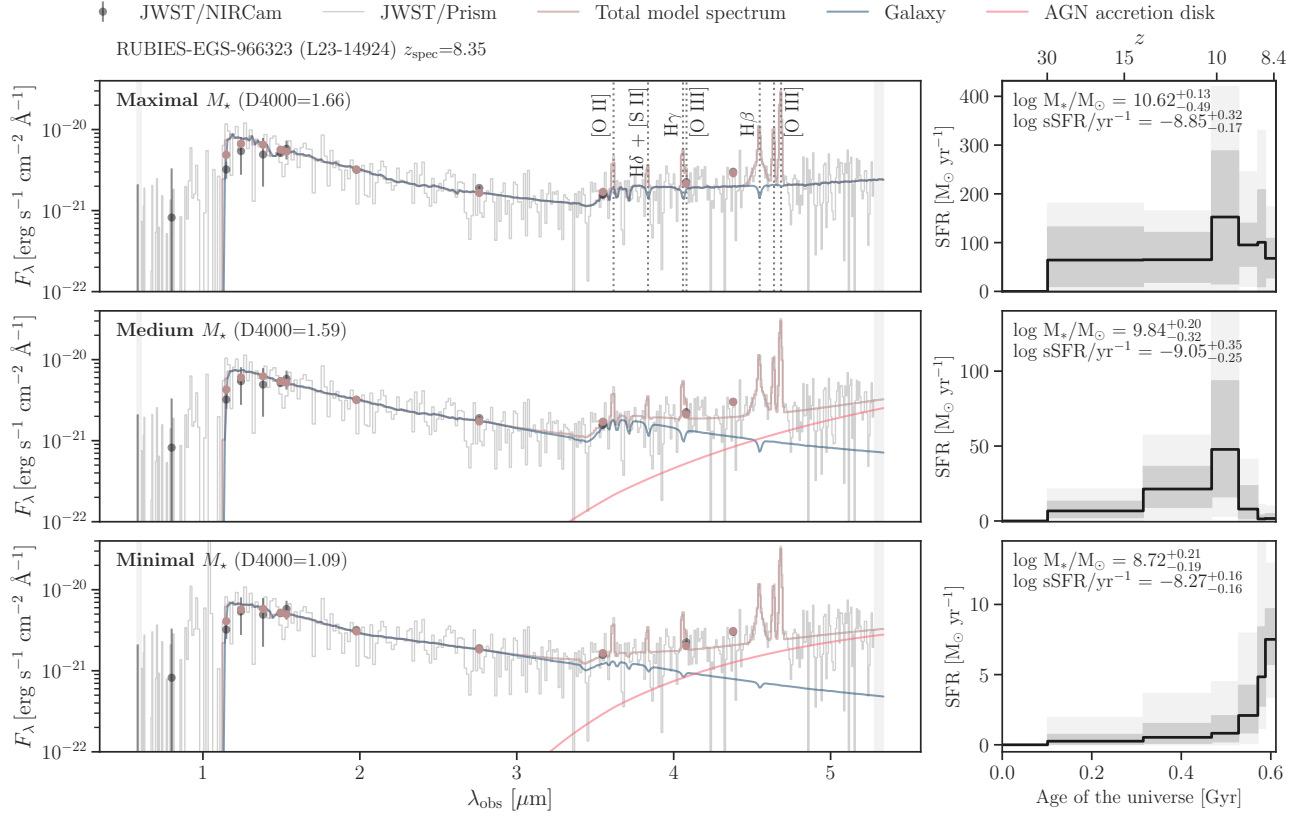


Figure 3-c. Spectrophotometric modeling for RUBIES-EGS-966323 (identified as 14924 in L23), with format as described in Figure 3-a.

6.1. Apparent Wavelength-dependent Contribution of AGN and Stellar Light

The models with minimal and medium stellar contribution infer that the AGN accretion disk dominates the rest-optical, while starlight dominates the rest-UV and also the Balmer break (by necessity). The AGN emission is heavily attenuated by dust, resulting in the observed red color. The transition from stellar- to AGN-dominated light can in principle be corroborated by the wavelength-dependent morphology—an unresolved morphology is more indicative of AGN-dominated light. The presence of broad emission lines is both a suggestion of AGN activity and, if these broad lines are AGN-powered as opposed to e.g., a stellar-driven outflow, they can put a soft lower limit on the AGN continuum contribution. This is because the AGN-powered broad $H\alpha$ EWs are typically observed to be $\lesssim 1000$ Å (more discussion of this point in Section 7); decreasing the AGN contribution to the continuum underneath these broad lines requires correspondingly higher AGN EWs, potentially outside of the previously observed range, which would require different and new AGN physics.

We find unambiguous broad $H\beta$ lines with FWHM > 2500 km s $^{-1}$ in RUBIES-EGS-49140 and 55604, which would be unusual for stellar-driven outflows (see [Veilleux et al. 2005](#) for an overview, or e.g., [Heckman et al. 2015](#); [Wang et al. 2020](#) for local starbursts). Stellar-driven outflows would typically also be seen in the forbidden lines, which are narrow in these objects—though it is possible for the outflowing gas to be sufficiently dense that it is not luminous in the forbidden lines. A broad component is marginally detected in RUBIES-EGS-966323 (§ 4). Additionally, we compare the observed $H\alpha$ EW to previous samples of LRDs. RUBIES-EGS-49140 and 55604 show large observed EWs of > 600 Å. We re-estimate the EW using the AGN continuum from the SED fits. Assuming the broad $H\alpha$ is originated from an AGN, the intrinsic EW must be larger in the models where considerable galaxy light contributes to the continuum near $H\alpha$. As seen from Figure 4, the increased EWs at the AGN continuum inferred from the medium stellar model are still roughly consistent with the distributions measured from a grism-selected LRD sample

Table 1. Inferred AGN and Host Galaxy Properties, and Emission Line Kinematics

	RUBIES-EGS-49140	RUBIES-EGS-55604	RUBIES-EGS-966323
ID in L23	—	38094	14924
RA [deg]	214.892248	214.983026	214.876149
DEC [deg]	52.877410	52.956001	52.880831
z_{phot} in L23	—	$7.48^{+0.04}_{-0.04}$	$8.87^{+0.13}_{-0.09}$
z_{spec}	$6.68351^{+0.00011}_{-0.00009}$	$6.98173^{+0.00013}_{-0.00012}$	$8.35304^{+0.00015}_{-0.00015}$
$\log M_{\star}/M_{\odot}$ (max M_{\star})	$11.17^{+0.15}_{-0.14}$	$11.07^{+0.15}_{-0.16}$	$10.62^{+0.13}_{-0.49}$
$\log M_{\star}/M_{\odot}$ (med M_{\star})	$9.93^{+0.22}_{-0.14}$	$9.79^{+0.14}_{-0.14}$	$9.84^{+0.20}_{-0.32}$
$\log M_{\star}/M_{\odot}$ (min M_{\star})	$9.50^{+0.08}_{-0.09}$	$8.99^{+0.16}_{-0.14}$	$8.72^{+0.21}_{-0.19}$
$\log Z/Z_{\odot}$	$-1.22^{+0.20}_{-0.22}$	$-0.50^{+0.28}_{-0.32}$	$-1.21^{+0.36}_{-0.41}$
Mass-weighted age [Gyr]	$0.21^{+0.06}_{-0.05}$	$0.22^{+0.04}_{-0.04}$	$0.22^{+0.03}_{-0.05}$
SFR ₁₀₀ [$M_{\odot} \text{ yr}^{-1}$]	$30.69^{+21.15}_{-13.37}$	$16.80^{+4.69}_{-4.36}$	$11.06^{+7.24}_{-5.57}$
$\log \text{sSFR}_{100}/\text{yr}^{-1}$	$-8.70^{+0.19}_{-0.28}$	$-8.95^{+0.14}_{-0.22}$	$-9.05^{+0.35}_{-0.25}$
$n_{\text{dust},2}$	$-0.21^{+0.22}_{-0.23}$	$-0.63^{+0.22}_{-0.22}$	$-0.42^{+0.21}_{-0.20}$
$\hat{\tau}_{\text{dust},2}$	$0.63^{+0.41}_{-0.24}$	$0.27^{+0.13}_{-0.08}$	$3.21^{+0.59}_{-0.78}$
$n_{\text{dust},4}$	$-1.69^{+0.14}_{-0.08}$	$-1.68^{+0.11}_{-0.08}$	$-1.38^{+0.20}_{-0.16}$
$\hat{\tau}_{\text{dust},4}$	$3.17^{+0.39}_{-0.33}$	$3.52^{+0.31}_{-0.36}$	$3.01^{+0.55}_{-0.73}$
$f_{\text{agn},7500\text{\AA}}$	$5.97^{+1.56}_{-1.64}$	$4.20^{+1.60}_{-1.10}$	$14.59^{+6.91}_{-6.21}$
σ (H β , broad) [km s^{-1}]	1402^{+79}_{-68}	1527^{+115}_{-106}	1369^{+315}_{-280} [†]
σ ([O III], narrow) [km s^{-1}]	68^{+17}_{-30}	48^{+20}_{-27} *	69^{+15}_{-27}

* Narrow component of the two-component fit to the [O III] line.

[†] Ambiguous broad component.

NOTE—For the inferred model parameters excluding the stellar mass, only those from the medium-stellar model are included.

at lower redshifts (Matthee et al. 2024), although at the higher end.

Furthermore, we can predict H α fluxes from the galaxy, given the inferred stellar population parameters, which provide another leverage on interpreting the continuum emission. For all three SED models, the predicted H α fluxes are at least 1 order of magnitude lower than the observed flux. This means that the SFRs in all models are much lower than the observed total H α flux, i.e., none of the stellar components in these models can be ruled out by requiring star formation which produces more H α flux than is observed.

Next, we cross-check the morphologies of RUBIES-EGS-55604 and 966323 as studied in Baggen et al. (2023). RUBIES-EGS-55604 (L23-38094) is among the most compact in L23, which is unresolved in the LW filters (< 0.22 kpc), but clearly exhibits two components in F115W and F150W. RUBIES-EGS-966323 is also unresolved in F444W, and likely resolved in F200W, although the F200W data is too faint to have a robust size estimate. Preliminary analysis on RUBIES-EGS-49140 reveals the same trend. A thorough study on the morphologies will be presented in Baggen et al. in prep.

These findings again indicate the presence of a transition from stellar to AGN light near the spectral break, thus favoring the minimum/medium stellar models.

6.2. Inferred Formation Histories

The inferred SFHs based on the three SED models are shown in Figure 3-a–3-c. All models have significant SFHs extending over hundreds of millions of years, necessary to produce the evolved stellar populations responsible for the Balmer breaks. However, there is some variation in the timescales of star formation, and significant variation in the amplitudes. The medium and maximal-stellar models require significant star formation at $z = 10$ and a recent decline in the SFR. The decline may be representative of a very early termination in star formation necessary to produce the very old galaxies observed at lower redshifts (Carnall et al. 2023; Glazebrook et al. 2024) or a more temporary mini-quenching event (Looser et al. 2023); however, we note that at least two of these Balmer breaks are substantially stronger than the Looser et al. (2023) break, implying a correspondingly longer period of quiescence ($\gtrsim 100$ Myr) than a mini-quenching event.

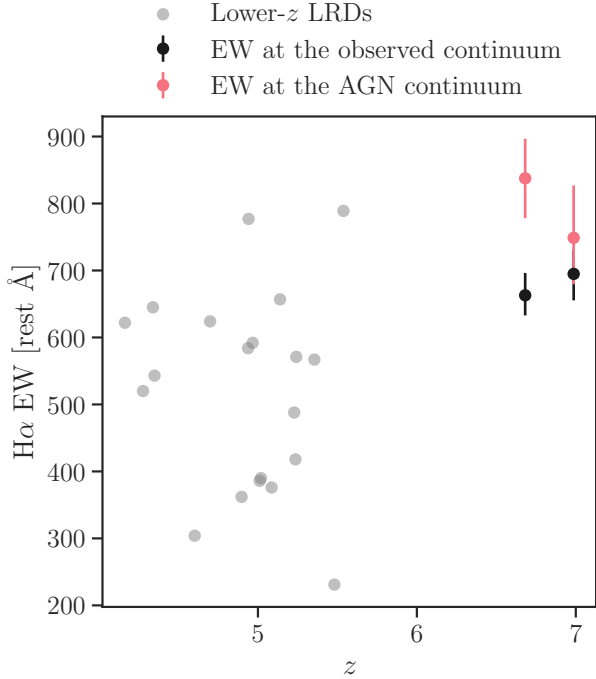


Figure 4. Rest-frame equivalent widths of $H\alpha$. EWs of the broad component of $H\alpha$ measured for the sample of this paper at the total continuum and AGN continuum (assuming the minimal stellar model) are represented in black and red, respectively. For reference, the EWs of a grism-selected LRD sample are plotted in gray (Matthee et al. 2024). Assuming the broad lines trace the AGN, then the implied EW at the AGN continuum in the case of starlight dominating the rest optical would be orders of magnitudes higher than the observed EW. Conversely, an AGN-dominated interpretation puts the EWs of our sample in a similar range as the grism-selected LRD sample.

Conversely, the minimal-stellar models decrease the strength of the stellar Balmer breaks by assuming a very red AGN continuum underneath, and in this way can infer purely rising SFHs for RUBIES-EGS-55604 and 966323. The signature of a recent decline in the SFH is still preserved in the brightest source, RUBIES-EGS-49140, which also has the strongest Balmer break among the three. This is an expected behavior—the less prominent Balmer breaks may be fit with a weaker break and steeper AGN continuum emission as the prior drives to minimize the stellar mass. However, it is worth emphasizing that this scenario hinges on a peculiar AGN continuum shape, which coincidentally aligns perfectly with that of the host galaxy to produce the observed spectral break. Alternatively, if not all the UV light is from stars, (e.g., scattered light from the AGN; Greene

et al. 2024), this would remove an important constraint pushing the inferred stellar ages younger, and perhaps relax the stringent requirement on the galaxy and the AGN conspiring to create a spectral break by allowing an older stellar population.

Interestingly, the maximal-stellar interpretation produces greater consistency with several massive, very old quiescent galaxies recently discovered with JWST at $z = 3 - 5$ (Carnall et al. 2023; Glazebrook et al. 2024; de Graaff et al. 2024a), as illustrated in Figure 5. Such coincidence may serve as an argument in favor of the maximal-stellar model.

Given the number density of the three objects in this work (a lower limit of $\sim 10^{-5} \text{ Mpc}^{-3}$), and e.g., the low number density of RUBIES-EGS-QG-1 ($\sim 5 \times 10^{-6} \text{ Mpc}^{-3}$; de Graaff et al. 2024a), it appears that the extreme red objects at $z = 7 - 8$ being massive are rare occurrences. However, the most straightforward prediction stemming from the discoveries of these low- z quiescent galaxies is the presence of Balmer breaks at $z = 7 - 8$, suggesting very early and/or rapid formation. While the number density may be low, they are indicative of a class of objects with early and rapid formation.

6.3. Contribution to the Cosmic Stellar Mass Density

One of the key results from L23 is that the high stellar masses in these objects suggest they dominate not just the high-mass end of the pre-JWST UV-selected galaxy stellar mass function (Stefanon et al. 2021), but indeed the entire stellar mass budget at this cosmic epoch. We revisit this point by estimating the cumulative stellar mass density using the stellar masses inferred in this work. Specifically, we bin the three objects into two redshift ranges, and sum the mass in each bin. The cosmic volume is estimated by integrating between the redshift limits over the areal coverage of CEERS (88.1 arcmin^2 ; Finkelstein et al. 2023). As in L23, we only consider the Poisson uncertainty and cosmic variance, and neglect corrections for incompleteness, given that any correction for incompleteness would increase the inferred stellar mass densities.

Figure 6 shows the cumulative stellar mass density in these objects compared to rest UV-selected objects. Importantly, rest-UV selection would fail to select any of the objects in this paper, which are extremely red: the total mass density is thus inferred to be the sum of the two (independent) curves. Although stellar mass functions incorporating the JWST observations have been estimated (e.g., Harvey et al. 2024; Weibel et al. 2024), the unclear physical nature of the reddest objects makes it especially difficult to both estimate and interpret the high-mass end of the high-redshift stellar mass func-

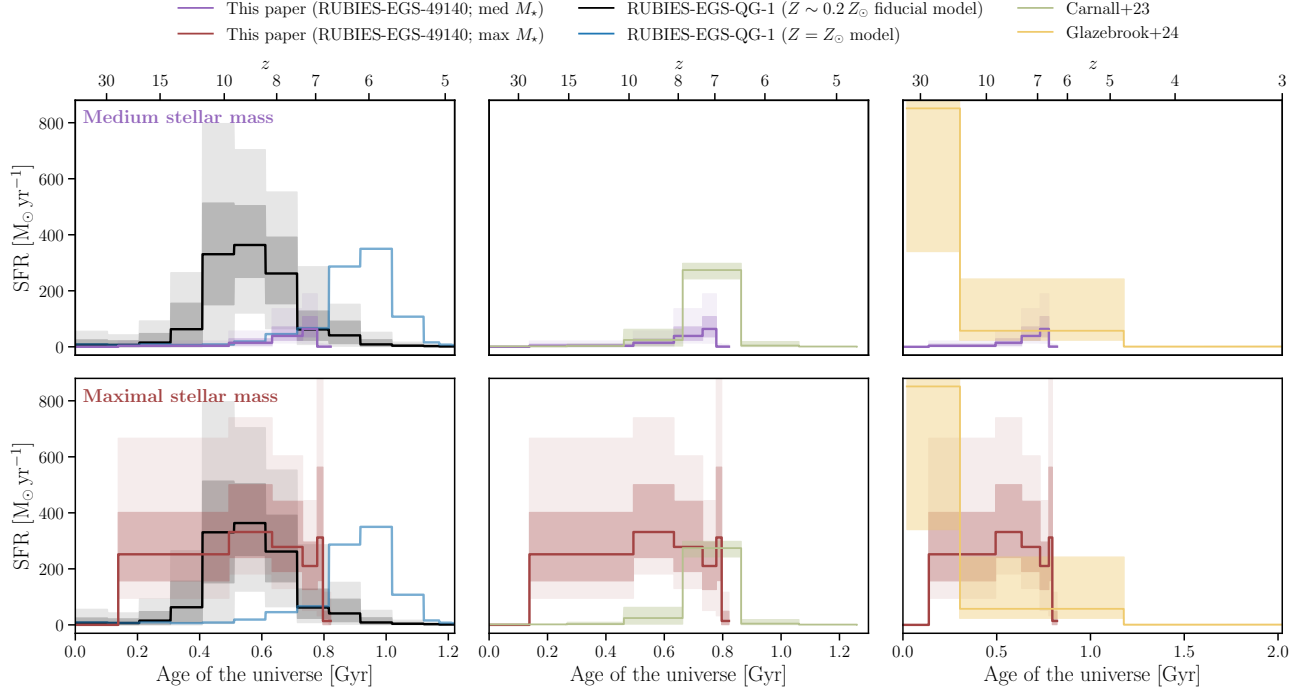


Figure 5. Formation history inferred for RUBIES-EGS-49140, compared to those inferred for maximally old quiescent galaxies at $z \sim 3 - 5$. From left to right, we show the SFHs of RUBIES-EGS-QG-1 (at $z = 4.9$ with $10^{11} M_{\odot}$; [de Graaff et al. 2024a](#)), GS-9209 (at $z = 4.7$ with $4 \times 10^{10} M_{\odot}$; [Carnall et al. 2023](#)), and ZF-UDS-7329 (at $z = 3.2$ with $10^{11} M_{\odot}$; [Glazebrook et al. 2024](#)). For the the $z = 4.9$ galaxy, we include the fiducial low-metallicity solution in black, with 1σ and 2σ uncertainties shaded in grey, and also an alternative solution assuming a solar metallicity in blue. For the other two quiescent galaxies, we only show the 1σ uncertainty. The top panels show the formation history from our medium-stellar model while the bottom panels show the formation history from our maximal-stellar model. A stellar interpretation of the light in RUBIES-EGS-49140 produces greater consistency with the massive quiescent galaxies, while the medium model fails to predict sufficient stellar mass to connect RUBIES-EGS-49140 to these massive old populations at lower redshift.

tions. We thus compare only to the pre-JWST UV-selected mass functions, as a test of what a rest-UV selection function may have missed.

Assuming the medium-stellar model, our analysis suggests that at $z \sim 7 - 8$, there are 20 – 50% of the total stellar mass density in this small population as in the entire rest-UV selected galaxy population, implying that $\sim 20 - 50\%$ of star formation at $z > 7$ occurs in the progenitors of these optically red objects and that they would dominate the high-mass end of the mass function. Adapting the minimal-stellar model, these objects comprise a much smaller $\sim 1\%$ of the cosmic mass budget and live in much more typical galaxies. Given that the Balmer break objects may have slowing or declining star formation histories, whereas UV-selected galaxies typically have rising formation histories by nature, this fraction is likely to be even higher at higher redshifts.

For reference, the number density of our sample is more than an order of magnitude lower than the total number density of the rest-UV selected sample, obtained

by integrating the Schechter fits down to a stellar mass limit of $10^8 M_{\odot}$ ([Stefanon et al. 2021](#)). This reinforces that the Balmer break objects may host disproportionately high levels of past star formation compared to the general galaxy population.

6.4. Dynamical Mass

While the Balmer lines are very broad, the forbidden lines are relatively narrow: the [O III] line widths for the three galaxies are FWHM $\sim 160, 113$, and 162 km s^{-1} (Table 1). As gas is viscous, the forbidden lines likely originate in disks, and—assuming those disks trace the gravitational potential of the galaxies—can be used to derive dynamical masses. As discussed in, e.g., [Förster Schreiber et al. 2014](#); [van Dokkum et al. 2015](#); [Price et al. 2016](#), the conversion from line width to dynamical mass depends on the spatial distribution of the gas, the orientation of the disks, and the orientation of the slit with respect to the rotation axis. While the gas is certainly compact (based on 2D spectra, where [O III]

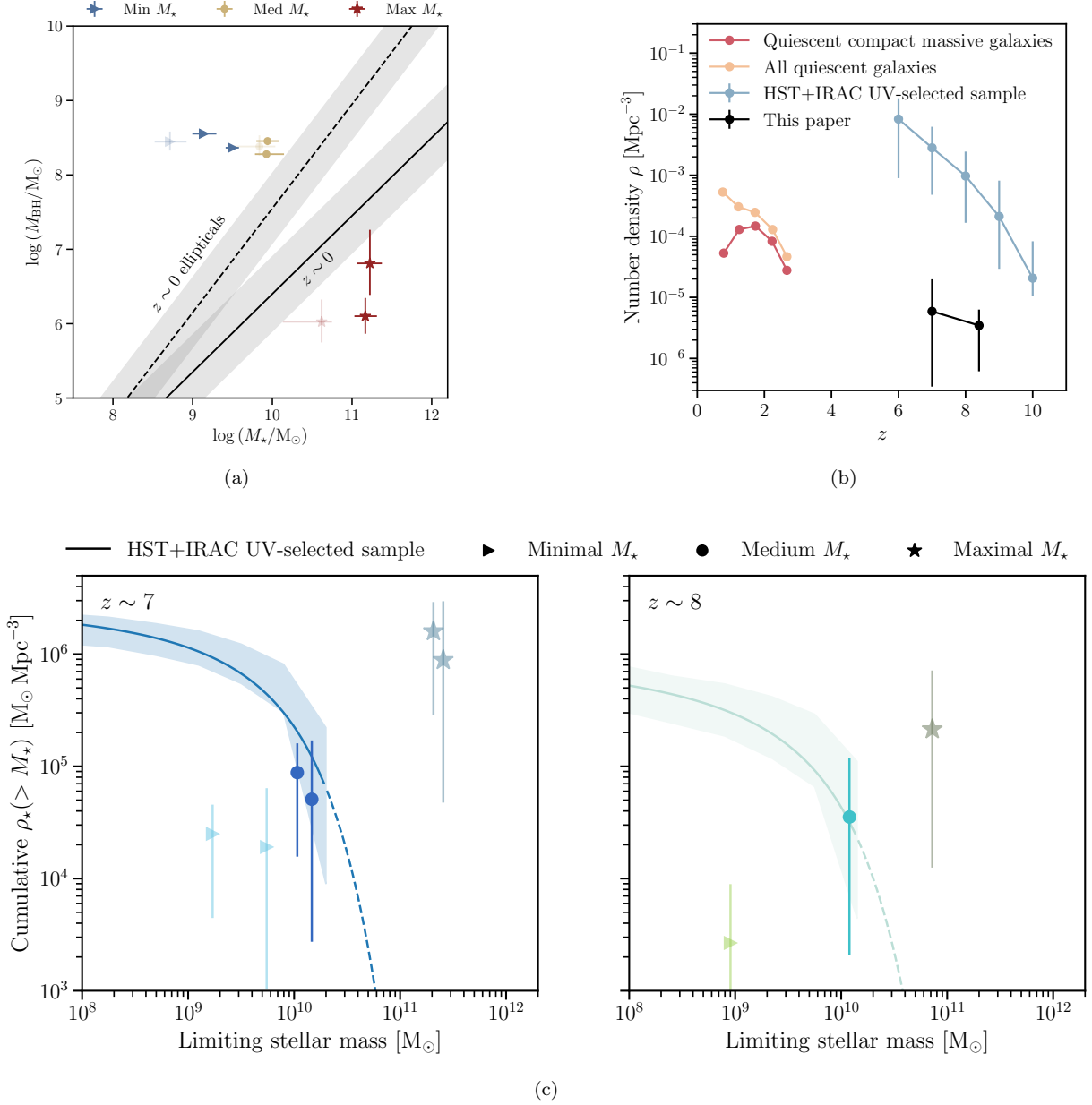


Figure 6. Implied population-level characteristics. (a) Stellar–black hole mass scaling relation. The local relation is plotted as a solid line, with the gray shading indicating the intrinsic scatter, whereas that derived for the elliptical galaxies and spiral/S0 galaxies with classical bulges is shown as a dashed line (Reines & Volonteri 2015). Over-plotted are the black hole masses estimated from L_{5100} and the broad $H\beta$ lines, and their corresponding stellar mass inferred from three SED models. The semi-transparent points indicate RUBIES-EGS-966323 for which the presence of a broad line is ambiguous. The black masses are uncertain as the inferred AGN luminosity from the SED models vary. (b) Number density, ρ . The red and orange curves are taken from van Dokkum et al. (2015). The blue curve is the total ρ for UV-selected sample, obtained by integrating the Schechter fits down to $10^8 M_{\odot}$ (Stefanon et al. 2021). ρ for the sample of this paper, in two redshift bins ($z < 7.0$, and $z \geq 7.0$), are shown in black; uncertainties reflect Poisson statistics and cosmic variance (Gehrels 1986). ρ of the Balmer break sample are comfortably below that of the $z = 3$ compact quiescent cores, although to answer whether the ρ of our objects match that of massive quiescent galaxies at later times would require a larger area and/or a more well-defined selection function. (c) Cumulative cosmic stellar mass density, ρ_{\star} . The curves are derived from the same Schechter fits, with the extrapolated regions indicated in dash. ρ_{\star} from this work are reported for the three SED models. Uncertainties again reflect Poisson statistics and cosmic variance. To facilitate a direct comparison to the literature, we adjust all our Chabrier stellar masses by +0.24 dex to Salpeter masses (Salpeter 1955). While the number density of the Balmer break sample is low, the mass density in these objects at least comprise $\sim 1\%$ of the cosmic mass budget. With the medium-stellar model, their contribution is roughly equal to the mass density in all UV-selected objects combined. Note that we do not attempt to account for selection effects, so all the reported densities for our sample should be taken as lower limits.

lines have about the same point-like morphology as the Balmer lines), the latter two dependencies are both unknown.

Nevertheless, it is instructive to estimate the dynamical mass. Following [van Dokkum et al. \(2015\)](#), we have

$$M_{\text{dyn}} = 2 \frac{V_{\text{rot}}^2 r_e}{G}, \quad (2)$$

where r_e is the spatial scale, taken to be ~ 100 pc ([Baggen et al. 2023](#)), and V_{rot} is the rotation velocity derived via

$$V_{\text{rot}} = \frac{\sigma_{\text{gas}}}{\alpha \sin^{-1}(i)}. \quad (3)$$

Assuming $\alpha = 0.8$ ([Rix et al. 1997](#); [Weiner et al. 2006](#)), and an inclination angle, i , of 45 degrees, the dynamical masses for RUBIES-EGS-49149, 55604, and 966323 are $\sim 10^{8.6}$, $10^{8.3}$, and $10^{8.6} M_{\odot}$, respectively, all at the low end of the stellar mass estimates, and actually in some tension with the black hole mass estimates alone (discussed in the next section).

Higher masses are possible if the gas has a larger spatial extent than the stars ([van Dokkum et al. 2015](#)), though the [O III] emission lines appear to have a highly compact morphology in the 2D spectra. Importantly, the LSF of NIRSpect is strongly dependent on morphology (up to a factor of ≈ 2 difference in resolution between a point source and uniformly-illuminated slit; [de Graaff et al. 2024b](#)). Therefore, if the source were to have $r_e \sim 1$ kpc, then σ_{gas} would decrease to $< 30 \text{ km s}^{-1}$; that is, by making the source larger, the dynamical mass remains similarly small. Low disk inclinations can also increase the dynamical mass. This is unlikely to be the case by chance, but it could result from selection effects; the red color selection may preferentially select obscured AGNs at particular down-the-barrel (i.e., face-on) orientations. However, given the significant inferred dust attenuation, a down-the-barrel orientation would be in some tension with the standard AGN model.

6.5. Galaxy–Black Hole Scaling Relationship

Figure 6-a compares the stellar mass–black hole mass relationship inferred for these objects to the local relationships. Based on our minimal/medium stellar masses, these objects host massive black holes $\sim 10\times$ above the $z = 0$ $M_{\star} - M_{\text{BH}}$ relationship ([Reines & Volonteri 2015](#)). The minimal stellar mass model is well above the typical scatter in this relationship, while the medium model is within $\sim 2\sigma$. These results align with previous findings on single objects ([Furtak et al. 2023](#); [Kokorev et al. 2023](#)), quasars ([Stone et al. 2024](#)), as well as that a $z \sim 5$ AGN sample which is located $\sim 10 - 100\times$

above the local relationship ([Pacucci et al. 2023](#)). At face value, this implies that these black holes are over-massive relative to their stellar components, and that the stellar components must continue to grow over the next 13 Gyr in order to produce the relationship observed today. However, we caution that the selection bias, where the luminous and massive black holes with emission sufficiently dominating their host galaxy are more readily observed in a flux-limited survey ([Lauer et al. 2007](#)), is likely exacerbated by the high-redshift frontier.

Meanwhile, the maximal stellar model predicts an AGN continuum orders of magnitudes lower than the galaxy continuum, and hence implies much lower black masses using the L_{5100} relation. Alternatively, since this model effectively predicts starlight dominating over all the observed wavelength range, it may be possible that these galaxies do not host AGNs at all, which is reasonable given the non-detection in X-rays ([Ananna et al. 2024](#); [Yue et al. 2024](#)). This then would perhaps require some yet-to-be-understood mechanism to produce the broad emission lines - for example, broad emission lines from supernovae have been previously mistaken for quasar activity ([Aretxaga et al. 1999](#)), though it remains unclear why SNe would be consistently associated with the other spectral characteristics of these objects.

While it is instructive to put our objects in the context of the $M_{\star} - M_{\text{BH}}$ relationship, despite substantial uncertainty in both the black hole and galaxy mass, we note that the $z \gtrsim 7$ objects do not necessarily need to lie on $z = 0$ relationship. [Peng \(2007\)](#) proposed that a large number of mergers lead to a statistical convergence process, and thus the slope of the $M_{\star} - M_{\text{BH}}$ relationship always becomes ~ 1 , regardless of the initial condition. In any case, the above scenarios all point to very different pictures of the early $M_{\star} - M_{\text{BH}}$ relationship and the subsequent evolution required to match the local scaling laws.

7. DISCUSSION AND CONCLUSIONS

Having discussed the implications of the physical properties and the formation histories resulting from each model, we now attempt to tie all the pieces together. We begin this section by briefly summarizing the modeling results, and then examine two potential interpretations of the nature of these objects.

7.1. A Brief Summary of the Implications of Different Stellar Contributions

The maximal stellar model, if correct, would have a remarkable impact on the first billion years of galaxy evolution. It proposes that the cumulative stellar mass

densities in these objects is comparable to that of all the UV-selected objects at these redshifts (Figure 6). Such early and efficient formation would be in tension with the standard assumption on the baryon to stellar conversion efficiency (Boylan-Kolchin 2023). Yet such an interpretation is consistent with the very old stellar populations observed in high-mass galaxies at $z = 3 - 5$ (Figure 5)—these require rapid, early assembly of $\gtrsim 10^{10.5} M_{\odot}$ in stellar mass, followed by an early cessation in star formation. The SEDs of their progenitors would look much like these objects—though these objects are $\sim 10\times$ smaller in physical size than these later quiescent galaxies.

In contrast, the models with minimal and medium stellar contributions (which in turn imply larger fractional AGN contributions) are supported by the observations of broad emission lines and compact morphologies at redder wavelengths. They require the black hole continuum to be steeply rising in the rest-optical, such that a rapid transition from a stellar-dominated continuum to a black hole-dominated continuum occurs. Furthermore, barring line-of-sight or other arguments, the small dynamical mass is in distinct tension with all models except the minimal stellar contribution. Meanwhile, the medium stellar model leads to a $M_{\star} - M_{\text{BH}}$ relation in less tension with (or requiring fewer mergers to become consistent with) the local relations.

7.2. Progenitors of Massive Quiescent Galaxies, or Low-mass Galaxies with Bright Black Holes?

It has long been suspected that the cores of the most massive galaxies in the local universe formed in a spectacular early burst of star formation at $z \gtrsim 5$, followed by an immediate and permanent quenching. This is underpinned by their high α -element abundances and their old (but unresolved) ages (e.g., Thomas et al. 2005; Conroy et al. 2014), and from number density analysis of massive, dense galaxy cores at $z = 0 - 3$ (van Dokkum et al. 2015).

Further evidence has risen to support this interpretation in the JWST era, in the form of “maximally old” quiescent galaxies identified at $z = 3 - 5$ with formation redshifts $z > 10$ (Glazebrook et al. 2024), $z \sim 10$ (de Graaff et al. 2024a) and $z \sim 8$ (Carnall et al. 2023). The higher redshift these objects are observed at allows for better resolution of the formation timescales, due to the younger age of the universe. This puts the formation of at least some of these massive galaxies in the first 500–600 Myr after the Big Bang. These objects have high stellar masses of $0.4 - 1 \times 10^{11} M_{\odot}$, and must have quenched shortly after the formation of the bulk of

their stellar mass, but likely progenitors have yet to be conclusively identified at this epoch.

The above gap in the observed evolution of massive quiescent galaxies could be bridged by these objects, if the formation history inferred from the maximal stellar model is correct (Figure 5). A key question is whether the number densities of these objects match the number densities of massive quiescent galaxies at later times. Answering this question requires a larger area and/or a more well-defined selection function; for now we simply note that the number densities of these objects are comfortably below the number density of $z = 3$ compact quiescent cores (van Dokkum et al. 2015). The presence of Balmer breaks at $z = 7 - 8$, indicating very early and/or rapid formation, is probably the most straightforward prediction from finding “maximally old” $z = 2 - 5$ quiescent galaxies. While the number density of these objects may be low, they are indicative of a class of objects with early and rapid formation. In addition, the strong spectroscopic selection effect, which we do not attempt to account for in this work, suggests that the value of $\sim 10^{-5} \text{ Mpc}^{-3}$ (Figure 6) is a lower limit of this class of objects. This is a key and perhaps convincing argument that in at least some of these objects, the stellar mass could be high (i.e., the AGN emission contribution to the continuum in the minimal/medium stellar models may be overestimated).

Another distinguishing property of the class of low- z massive quiescent galaxies is the remarkable compactness and high stellar densities, with effective radii of 1 kpc or less at $z \sim 2$ (van Dokkum et al. 2008). Baggen et al. (2023) showed that a fully stellar interpretation as presented in L23 (or similarly, the maximal stellar model of this paper) yields similar stellar densities to the cores observed at later times, albeit with significantly smaller sizes, by a factor of 10.

In addition, the enhanced SFR inferred from the maximal stellar model would explain the surprising overabundance of luminous galaxies at $z \gtrsim 10$ (e.g., Atek et al. 2023; Casey et al. 2024; Finkelstein et al. 2023; Robertson et al. 2023). Their dense stellar structures would presumably be formed from very dense gas associated with highly efficient star formation (Schmidt 1959; Kennicutt 1998), perhaps in a similar manner as the super-star clusters with unusually high cloud surface densities in the local universe (Smith et al. 2006; Turner et al. 2015).

Finally, the greater stellar mass case may be preferred on the grounds that it does not require a conveniently located AGN continuum to account for the observed spectral break. As the stellar mass decreases, so does the Balmer break strength in the galaxy spec-

trum, meaning that the AGN continuum must precisely match the shape and intensity needed to replicate the spectral break.

Therefore, we conclude that one possible interpretation is that the high-redshift Balmer break sample presented in this work are the progenitors of the first massive galaxies, observed directly after their rapid co-formation with their supermassive black holes. Certainly, this interpretation leaves difficult problems. We discuss the outstanding questions below, in connection with an alternative interpretation of these objects being low-mass galaxies hosting AGNs.

To start, it is not intuitive to explain the broad emission lines with a non-AGN origin, since stellar-driven scenarios are seemingly inconsistent with the lack of velocity offset between the narrow and broad emission line components, and the symmetry of the lines. However, all the spectroscopically confirmed LRDs, which share similar but non-identical SED shapes as our sample, are under-luminous in X-ray (Furtak et al. 2023; Greene et al. 2024; Maiolino et al. 2023; Kocevski et al. 2023; Matthee et al. 2024; Wang et al. 2024a). More recently, most LRDs are found to be under-detected in X-ray in Chandra observations (Ananna et al. 2024; Yue et al. 2024). It perhaps is then fair to speculate alternative, non-AGN-driven physical causes.

Second, the implied formation is uncomfortably early and efficient, compared to the conventional assumption on the baryon to stellar conversion efficiency (Boylan-Kolchin 2023). Paradoxically, the cores of local massive galaxies appear to have bottom-heavy stellar initial mass functions (e.g., Conroy & van Dokkum 2012), with some evidence that this persists or even strengthens at $z \sim 2$ (van Dokkum et al. 2024, though see Mercier et al. 2023 for an alternate take). This would increase the inferred stellar masses (without changing the observed SED in any way; Wang et al. 2024c) by a factor of a few, further increasing the tension with the cosmic baryon fraction.

Third, the objects of this work are remarkably compact ($r_e \lesssim 0.1$ kpc; Baggen et al. 2023). This is even more striking when comparing to RUBIES-EGS-QG-1, which has $r_e \sim 0.6$ kpc (de Graaff et al. 2024a), and the $z \sim 2 - 3$ compact quiescent galaxies, which are likewise much larger (by a factor of ~ 10 ; van Dokkum et al. 2015). At face value, the stellar bodies of these objects would have to rapidly expand over the subsequent few hundred million years. Additionally, it is difficult to imagine a massive galaxy being less than 100 pc in size. This would indicate an increased importance for dynamical evolution effects normally reserved for dense globular clusters (Spitzer 1987; Vesperini & Heggie 1997), e.g., segregation by mass, where the massive stars and bina-

ries tend to sink toward the cores, and the low-mass stars move outward into the halo. Interestingly, the mass segregation, if it happened, would change the initial mass distribution, and thus relieve the tension in inferring uncomfortably large stellar mass in the current models, without evoking a change in the form of the initial mass function.

Future deeper, and redder observations are critical to distinguishing between galaxy and AGN contributions to the continuum in this population. We elaborate on the lingering questions affecting the interpretation of our sample, along with possible ways forward, in the section below.

7.3. Key Remaining Questions About the Nature of the Balmer Break Sample

One remaining puzzle is the contrast between the broad Balmer lines and the narrow forbidden emission lines. While the line widths have been shown to correlate well with mass in statistical samples (Wuyts et al. 2016), narrow line widths in H α and CO have also been observed in some massive galaxies at $z \sim 2.3$ when there is considerably less ambiguity about the stellar masses (van Dokkum et al. 2015; Mowla et al. 2019). Possibly, these narrow line widths can be explained by some combination of face-on disks and peculiar gas geometry (i.e., the emitting gas is not associated with the deep stellar potential well). The discrepancy between the significantly lower dynamical mass compared to the inferred stellar mass from the medium/maximal stellar SED models of all three objects, coupled with the absence of available evidence indicating the existence of disks within them, make such an argument less satisfying. However, it remains possible that the color-based selection function selects for a particular face-on orientation angle.

As for the $M_\star - M_{\text{BH}}$ relation, we cautioned about the selection bias (Lauer et al. 2007) in Section 6.5. Recently it has been argued that over-massive black holes are not inconsistent with the local relation after taking in account the selection bias (Li et al. 2024). A well-defined selection function was one of the key pieces in designing the observation strategy for the RUBIES program, and we will perform a more complete population-level analysis in a future paper.

A key missing piece of evidence is deep MIRI imaging—the stellar-dominated and AGN-dominated models diverge at these wavelengths by a factor of $\sim 2 - 8$, as stellar light is expected to decline at longer wavelengths, whereas AGN emission is expected to show a flat spectrum (if deficient in hot dust; Williams et al. 2023; Pérez-González et al. 2024; Wang et al. 2024a) or

a rising spectrum (from a dusty torus). X-ray detections or firmer upper limits would also help to establish the AGN nature of these objects.

Finally, a word of caution: despite our exploration of several models, ranging from the minimal to maximal extremes of stellar mass, none of these models fully align with our current understanding of galaxy formation and evolution. This challenge arises from a combination of the difficulty in separating AGN and host galaxy light, and the ongoing debate surrounding evolutionary scenarios sparked by JWST’s discoveries of (potentially) over-massive black holes and massive quiescent systems. In light of all the complexities, the statements in this paper should all be considered contingent. There certainly remains ample room for reinterpretation in the future.

7.4. *Final Remarks*

JWST is revolutionizing our knowledge of the formation of early galaxies and their black holes. In this paper, we report a remarkable discovery of prominent Balmer breaks as early as $z_{\text{spec}} = 8.35$, and intriguingly, its co-existence with broad emission lines. The high-redshift Balmer breaks reveal unambiguously the presence of evolved stellar populations with extended formation histories within the first 600–800 Myr after the Big Bang. However, all of the examined explanations on the potential origins and evolutionary tracks for these objects leave key lingering questions. Deeper spectroscopic data revealing stellar absorption features, and JWST/MIRI data sampling the red continuum would further elucidate the nature of these intriguing objects. We conclude by emphasizing that observed Balmer breaks establishing the existence of evolved stellar populations with ex-

tended formation histories, presented herein mark an important development in understanding the origins and evolution of galaxies and their central supermassive black holes.

ACKNOWLEDGMENTS

B.W. and J.L. acknowledge support from JWST-GO-04233.009-A. The Cosmic Dawn Center is funded by the Danish National Research Foundation (DNRF) under grant #140. This research was supported by the International Space Science Institute (ISSI) in Bern, through ISSI International Team project #562 (First Light at Cosmic Dawn: Exploiting the James Webb Space Telescope Revolution). This work is based in part on observations made with the NASA/ESA/CSA James Webb Space Telescope. The data were obtained from the Mikulski Archive for Space Telescopes at the Space Telescope Science Institute, which is operated by the Association of Universities for Research in Astronomy, Inc., under NASA contract NAS 5-03127 for JWST. Computations for this research were performed on the Pennsylvania State University’s Institute for Computational and Data Sciences’ Roar supercomputer. This publication made use of the NASA Astrophysical Data System for bibliographic information.

Facilities: HST (ACS, WFC3), JWST (NIRCam, NIRSpec)

Software: Astropy (Astropy Collaboration et al. 2022), EAzy (Brammer et al. 2008), emcee (Foreman-Mackey et al. 2013), dynesty (Speagle 2020), Matplotlib (Hunter 2007), msaexp (Brammer 2023b), msafit (de Graaff et al. 2024b), NumPy (Harris et al. 2020), Prospector (Johnson et al. 2021),

REFERENCES

- Ananna, T. T., Bogdán, Á., Kovács, O. E., Natarajan, P., & Hickox, R. C. 2024, arXiv e-prints, arXiv:2404.19010. <https://arxiv.org/abs/2404.19010>
- Aretxaga, I., Joguet, B., Kunth, D., Melnick, J., & Terlevich, R. J. 1999, ApJL, 519, L123, doi: [10.1086/312114](https://doi.org/10.1086/312114)
- Assef, R. J., Denney, K. D., Kochanek, C. S., et al. 2011, ApJ, 742, 93, doi: [10.1088/0004-637X/742/2/93](https://doi.org/10.1088/0004-637X/742/2/93)
- Astropy Collaboration, Price-Whelan, A. M., Lim, P. L., et al. 2022, ApJ, 935, 167, doi: [10.3847/1538-4357/ac7c74](https://doi.org/10.3847/1538-4357/ac7c74)
- Atek, H., Chemerynska, I., Wang, B., et al. 2023, MNRAS, 524, 5486, doi: [10.1093/mnras/stad1998](https://doi.org/10.1093/mnras/stad1998)
- Baggen, J. F. W., van Dokkum, P., Labbé, I., et al. 2023, ApJL, 955, L12, doi: [10.3847/2041-8213/acf5ef](https://doi.org/10.3847/2041-8213/acf5ef)
- Bagley, M. B., Finkelstein, S. L., Koekemoer, A. M., et al. 2023, ApJL, 946, L12, doi: [10.3847/2041-8213/acbb08](https://doi.org/10.3847/2041-8213/acbb08)
- Balogh, M. L., Morris, S. L., Yee, H. K. C., Carlberg, R. G., & Ellingson, E. 1999, ApJ, 527, 54, doi: [10.1086/308056](https://doi.org/10.1086/308056)
- Barro, G., Trump, J. R., Koo, D. C., et al. 2014, ApJ, 795, 145, doi: [10.1088/0004-637X/795/2/145](https://doi.org/10.1088/0004-637X/795/2/145)
- Barro, G., Pérez-González, P. G., Kocevski, D. D., et al. 2024, ApJ, 963, 128, doi: [10.3847/1538-4357/ad167e](https://doi.org/10.3847/1538-4357/ad167e)
- Bezanson, R., van Dokkum, P. G., Tal, T., et al. 2009, ApJ, 697, 1290, doi: [10.1088/0004-637X/697/2/1290](https://doi.org/10.1088/0004-637X/697/2/1290)
- Binggeli, C., Zackrisson, E., Ma, X., et al. 2019, MNRAS, 489, 3827, doi: [10.1093/mnras/stz2387](https://doi.org/10.1093/mnras/stz2387)
- Blandford, R. D., & McKee, C. F. 1982, ApJ, 255, 419, doi: [10.1086/159843](https://doi.org/10.1086/159843)

- Boylan-Kolchin, M. 2023, *Nature Astronomy*, 7, 731, doi: [10.1038/s41550-023-01937-7](https://doi.org/10.1038/s41550-023-01937-7)
- Brammer, G. 2023a, grizli, 1.9.11, Zenodo, doi: [10.5281/zenodo.1146904](https://doi.org/10.5281/zenodo.1146904)
- . 2023b, msaexp: NIRSpec analysis tools, 0.6.17, Zenodo, doi: [10.5281/zenodo.7299500](https://doi.org/10.5281/zenodo.7299500)
- Brammer, G. B., van Dokkum, P. G., & Coppi, P. 2008, *ApJ*, 686, 1503, doi: [10.1086/591786](https://doi.org/10.1086/591786)
- Bruzual A., G. 1983, *ApJ*, 273, 105, doi: [10.1086/161352](https://doi.org/10.1086/161352)
- Calzetti, D., Armus, L., Bohlin, R. C., et al. 2000, *ApJ*, 533, 682, doi: [10.1086/308692](https://doi.org/10.1086/308692)
- Carnall, A. C., McLure, R. J., Dunlop, J. S., et al. 2023, *Nature*, 619, 716, doi: [10.1038/s41586-023-06158-6](https://doi.org/10.1038/s41586-023-06158-6)
- Casey, C. M., Akins, H. B., Shuntov, M., et al. 2024, *ApJ*, 965, 98, doi: [10.3847/1538-4357/ad2075](https://doi.org/10.3847/1538-4357/ad2075)
- Chabrier, G. 2003, *PASP*, 115, 763, doi: [10.1086/376392](https://doi.org/10.1086/376392)
- Choi, J., Dotter, A., Conroy, C., et al. 2016, *ApJ*, 823, 102, doi: [10.3847/0004-637X/823/2/102](https://doi.org/10.3847/0004-637X/823/2/102)
- Conroy, C., Graves, G. J., & van Dokkum, P. G. 2014, *ApJ*, 780, 33, doi: [10.1088/0004-637X/780/1/33](https://doi.org/10.1088/0004-637X/780/1/33)
- Conroy, C., & Gunn, J. E. 2010, *ApJ*, 712, 833, doi: [10.1088/0004-637X/712/2/833](https://doi.org/10.1088/0004-637X/712/2/833)
- Conroy, C., & van Dokkum, P. G. 2012, *ApJ*, 760, 71, doi: [10.1088/0004-637X/760/1/71](https://doi.org/10.1088/0004-637X/760/1/71)
- de Graaff, A., Setton, D. J., Brammer, G., et al. 2024a, arXiv e-prints, arXiv:2404.05683, doi: [10.48550/arXiv.2404.05683](https://doi.org/10.48550/arXiv.2404.05683)
- de Graaff, A., Rix, H.-W., Carniani, S., et al. 2024b, *A&A*, 684, A87, doi: [10.1051/0004-6361/202347755](https://doi.org/10.1051/0004-6361/202347755)
- D'Eugenio, F., Cameron, A. J., Scholtz, J., et al. 2024, arXiv e-prints, arXiv:2404.06531, doi: [10.48550/arXiv.2404.06531](https://doi.org/10.48550/arXiv.2404.06531)
- Dotter, A. 2016, *ApJS*, 222, 8, doi: [10.3847/0067-0049/222/1/8](https://doi.org/10.3847/0067-0049/222/1/8)
- Draine, B. T., & Li, A. 2007, *ApJ*, 657, 810, doi: [10.1086/511055](https://doi.org/10.1086/511055)
- Endsley, R., Stark, D. P., Whitler, L., et al. 2023, *MNRAS*, 524, 2312, doi: [10.1093/mnras/stad1919](https://doi.org/10.1093/mnras/stad1919)
- Ferrarese, L., & Merritt, D. 2000, *ApJL*, 539, L9, doi: [10.1086/312838](https://doi.org/10.1086/312838)
- Ferruit, P., Jakobsen, P., Giardino, G., et al. 2022, *A&A*, 661, A81, doi: [10.1051/0004-6361/202142673](https://doi.org/10.1051/0004-6361/202142673)
- Finkelstein, S. L., Leung, G. C. K., Bagley, M. B., et al. 2023, arXiv e-prints, arXiv:2311.04279, doi: [10.48550/arXiv.2311.04279](https://doi.org/10.48550/arXiv.2311.04279)
- Foreman-Mackey, D., Hogg, D. W., Lang, D., & Goodman, J. 2013, *PASP*, 125, 306, doi: [10.1086/670067](https://doi.org/10.1086/670067)
- Förster Schreiber, N. M., Genzel, R., Newman, S. F., et al. 2014, *ApJ*, 787, 38, doi: [10.1088/0004-637X/787/1/38](https://doi.org/10.1088/0004-637X/787/1/38)
- Furtak, L. J., Labbé, I., Zitrin, A., et al. 2023, arXiv e-prints, arXiv:2308.05735, doi: [10.48550/arXiv.2308.05735](https://doi.org/10.48550/arXiv.2308.05735)
- Gehrels, N. 1986, *ApJ*, 303, 336, doi: [10.1086/164079](https://doi.org/10.1086/164079)
- Glazebrook, K., Nanayakkara, T., Schreiber, C., et al. 2024, *Nature*, 628, 277, doi: [10.1038/s41586-024-07191-9](https://doi.org/10.1038/s41586-024-07191-9)
- Greene, J. E., Labbe, I., Goulding, A. D., et al. 2024, *ApJ*, 964, 39, doi: [10.3847/1538-4357/ad1e5f](https://doi.org/10.3847/1538-4357/ad1e5f)
- Grogin, N. A., Kocevski, D. D., Faber, S. M., et al. 2011, *ApJS*, 197, 35, doi: [10.1088/0067-0049/197/2/35](https://doi.org/10.1088/0067-0049/197/2/35)
- Hamilton, D. 1985, *ApJ*, 297, 371, doi: [10.1086/163537](https://doi.org/10.1086/163537)
- Harris, C. R., Millman, K. J., van der Walt, S. J., et al. 2020, *Nature*, 585, 357, doi: [10.1038/s41586-020-2649-2](https://doi.org/10.1038/s41586-020-2649-2)
- Harvey, T., Conselice, C., Adams, N. J., et al. 2024, arXiv e-prints, arXiv:2403.03908, doi: [10.48550/arXiv.2403.03908](https://doi.org/10.48550/arXiv.2403.03908)
- Hashimoto, T., Laporte, N., Mawatari, K., et al. 2018, *Nature*, 557, 392, doi: [10.1038/s41586-018-0117-z](https://doi.org/10.1038/s41586-018-0117-z)
- Heckman, T. M., Alexandroff, R. M., Borthakur, S., Overzier, R., & Leitherer, C. 2015, *ApJ*, 809, 147, doi: [10.1088/0004-637X/809/2/147](https://doi.org/10.1088/0004-637X/809/2/147)
- Heintz, K. E., Brammer, G. B., Watson, D., et al. 2024, arXiv e-prints, arXiv:2404.02211, doi: [10.48550/arXiv.2404.02211](https://doi.org/10.48550/arXiv.2404.02211)
- Hinshaw, G., Larson, D., Komatsu, E., et al. 2013, *ApJS*, 208, 19, doi: [10.1088/0067-0049/208/2/19](https://doi.org/10.1088/0067-0049/208/2/19)
- Hunter, J. D. 2007, *Computing in Science and Engineering*, 9, 90, doi: [10.1109/MCSE.2007.55](https://doi.org/10.1109/MCSE.2007.55)
- Jeffreys, H. 1961, *The Theory of Probability*, 3rd edn. (Oxford University Press)
- Johnson, B. D., Leja, J., Conroy, C., & Speagle, J. S. 2021, *ApJS*, 254, 22, doi: [10.3847/1538-4365/abef67](https://doi.org/10.3847/1538-4365/abef67)
- Kaspi, S., Smith, P. S., Netzer, H., et al. 2000, *ApJ*, 533, 631, doi: [10.1086/308704](https://doi.org/10.1086/308704)
- Kennicutt, Robert C., J. 1998, *ARA&A*, 36, 189, doi: [10.1146/annurev.astro.36.1.189](https://doi.org/10.1146/annurev.astro.36.1.189)
- Kocevski, D. D., Onoue, M., Inayoshi, K., et al. 2023, *ApJL*, 954, L4, doi: [10.3847/2041-8213/ace5a0](https://doi.org/10.3847/2041-8213/ace5a0)
- Kocevski, D. D., Finkelstein, S. L., Barro, G., et al. 2024, arXiv e-prints, arXiv:2404.03576, doi: [10.48550/arXiv.2404.03576](https://doi.org/10.48550/arXiv.2404.03576)
- Koekemoer, A. M., Faber, S. M., Ferguson, H. C., et al. 2011, *ApJS*, 197, 36, doi: [10.1088/0067-0049/197/2/36](https://doi.org/10.1088/0067-0049/197/2/36)
- Kokorev, V., Fujimoto, S., Labbe, I., et al. 2023, *ApJL*, 957, L7, doi: [10.3847/2041-8213/ad037a](https://doi.org/10.3847/2041-8213/ad037a)
- Labbé, I., van Dokkum, P., Nelson, E., et al. 2023a, *Nature*, 616, 266, doi: [10.1038/s41586-023-05786-2](https://doi.org/10.1038/s41586-023-05786-2)
- Labbé, I., Greene, J. E., Bezanson, R., et al. 2023b, arXiv e-prints, arXiv:2306.07320, doi: [10.48550/arXiv.2306.07320](https://doi.org/10.48550/arXiv.2306.07320)

- Landt, H., Ward, M. J., Peterson, B. M., et al. 2013, MNRAS, 432, 113, doi: [10.1093/mnras/stt421](https://doi.org/10.1093/mnras/stt421)
- Lauer, T. R., Faber, S. M., Richstone, D., et al. 2007, ApJ, 662, 808, doi: [10.1086/518223](https://doi.org/10.1086/518223)
- Leja, J., Johnson, B. D., Conroy, C., van Dokkum, P. G., & Byler, N. 2017, ApJ, 837, 170, doi: [10.3847/1538-4357/aa5ffe](https://doi.org/10.3847/1538-4357/aa5ffe)
- Li, J., Silverman, J. D., Shen, Y., et al. 2024, arXiv e-prints, arXiv:2403.00074, doi: [10.48550/arXiv.2403.00074](https://doi.org/10.48550/arXiv.2403.00074)
- Liddle, A. R. 2004, MNRAS, 351, L49, doi: [10.1111/j.1365-2966.2004.08033.x](https://doi.org/10.1111/j.1365-2966.2004.08033.x)
- Looser, T. J., D'Eugenio, F., Maiolino, R., et al. 2023, arXiv e-prints, arXiv:2302.14155, doi: [10.48550/arXiv.2302.14155](https://doi.org/10.48550/arXiv.2302.14155)
- Maiolino, R., Scholtz, J., Curtis-Lake, E., et al. 2023, arXiv e-prints, arXiv:2308.01230, doi: [10.48550/arXiv.2308.01230](https://doi.org/10.48550/arXiv.2308.01230)
- Matthee, J., Naidu, R. P., Brammer, G., et al. 2024, ApJ, 963, 129, doi: [10.3847/1538-4357/ad2345](https://doi.org/10.3847/1538-4357/ad2345)
- Mercier, W., Shuntov, M., Gavazzi, R., et al. 2023, arXiv e-prints, arXiv:2309.15986, doi: [10.48550/arXiv.2309.15986](https://doi.org/10.48550/arXiv.2309.15986)
- Mowla, L. A., Nelson, E. J., van Dokkum, P., & Tadaki, K.-i. 2019, ApJL, 886, L28, doi: [10.3847/2041-8213/ab54d1](https://doi.org/10.3847/2041-8213/ab54d1)
- Nelson, E., van Dokkum, P., Franx, M., et al. 2014, Nature, 513, 394, doi: [10.1038/nature13616](https://doi.org/10.1038/nature13616)
- Noll, S., Burgarella, D., Giovannoli, E., et al. 2009, A&A, 507, 1793, doi: [10.1051/0004-6361/200912497](https://doi.org/10.1051/0004-6361/200912497)
- Pacucci, F., Nguyen, B., Carniani, S., Maiolino, R., & Fan, X. 2023, ApJL, 957, L3, doi: [10.3847/2041-8213/ad0158](https://doi.org/10.3847/2041-8213/ad0158)
- Park, M., Belli, S., Conroy, C., et al. 2024, arXiv e-prints, arXiv:2404.17945, doi: [10.48550/arXiv.2404.17945](https://doi.org/10.48550/arXiv.2404.17945)
- Peng, C. Y. 2007, ApJ, 671, 1098, doi: [10.1086/522774](https://doi.org/10.1086/522774)
- Pérez-González, P. G., Barro, G., Rieke, G. H., et al. 2024, arXiv e-prints, arXiv:2401.08782, doi: [10.48550/arXiv.2401.08782](https://doi.org/10.48550/arXiv.2401.08782)
- Price, S. H., Kriek, M., Shapley, A. E., et al. 2016, ApJ, 819, 80, doi: [10.3847/0004-637X/819/1/80](https://doi.org/10.3847/0004-637X/819/1/80)
- Reines, A. E., & Volonteri, M. 2015, ApJ, 813, 82, doi: [10.1088/0004-637X/813/2/82](https://doi.org/10.1088/0004-637X/813/2/82)
- Rix, H.-W., Guhathakurta, P., Colless, M., & Ing, K. 1997, MNRAS, 285, 779, doi: [10.1093/mnras/285.4.779](https://doi.org/10.1093/mnras/285.4.779)
- Robertson, B., Johnson, B. D., Tacchella, S., et al. 2023, arXiv e-prints, arXiv:2312.10033, doi: [10.48550/arXiv.2312.10033](https://doi.org/10.48550/arXiv.2312.10033)
- Salpeter, E. E. 1955, ApJ, 121, 161, doi: [10.1086/145971](https://doi.org/10.1086/145971)
- Sánchez-Blázquez, P., Peletier, R. F., Jiménez-Vicente, J., et al. 2006, MNRAS, 371, 703, doi: [10.1111/j.1365-2966.2006.10699.x](https://doi.org/10.1111/j.1365-2966.2006.10699.x)
- Schmidt, M. 1959, ApJ, 129, 243, doi: [10.1086/146614](https://doi.org/10.1086/146614)
- Smith, L. J., Westmoquette, M. S., Gallagher, J. S., et al. 2006, MNRAS, 370, 513, doi: [10.1111/j.1365-2966.2006.10507.x](https://doi.org/10.1111/j.1365-2966.2006.10507.x)
- Speagle, J. S. 2020, MNRAS, 493, 3132, doi: [10.1093/mnras/staa278](https://doi.org/10.1093/mnras/staa278)
- Spitzer, L. 1987, Dynamical evolution of globular clusters
- Stefanon, M., Bouwens, R. J., Labbé, I., et al. 2021, ApJ, 922, 29, doi: [10.3847/1538-4357/ac1bb6](https://doi.org/10.3847/1538-4357/ac1bb6)
- Steinhardt, C. L., Kokorev, V., Rusakov, V., Garcia, E., & Sneppen, A. 2023, ApJL, 951, L40, doi: [10.3847/2041-8213/acdef6](https://doi.org/10.3847/2041-8213/acdef6)
- Stone, M. A., Lyu, J., Rieke, G. H., Alberts, S., & Hainline, K. N. 2024, ApJ, 964, 90, doi: [10.3847/1538-4357/ad2a57](https://doi.org/10.3847/1538-4357/ad2a57)
- Tacchella, S., Bose, S., Conroy, C., Eisenstein, D. J., & Johnson, B. D. 2018, ApJ, 868, 92, doi: [10.3847/1538-4357/aae8e0](https://doi.org/10.3847/1538-4357/aae8e0)
- Temple, M. J., Hewett, P. C., & Banerji, M. 2021, MNRAS, 508, 737, doi: [10.1093/mnras/stab2586](https://doi.org/10.1093/mnras/stab2586)
- Thomas, D., Maraston, C., Bender, R., & Mendes de Oliveira, C. 2005, ApJ, 621, 673, doi: [10.1086/426932](https://doi.org/10.1086/426932)
- Turner, J. L., Beck, S. C., Benford, D. J., et al. 2015, Nature, 519, 331, doi: [10.1038/nature14218](https://doi.org/10.1038/nature14218)
- Valentino, F., Brammer, G., Gould, K. M. L., et al. 2023, ApJ, 947, 20, doi: [10.3847/1538-4357/acbefa](https://doi.org/10.3847/1538-4357/acbefa)
- van Dokkum, P., Brammer, G., Wang, B., Leja, J., & Conroy, C. 2024, Nature Astronomy, 8, 119, doi: [10.1038/s41550-023-02103-9](https://doi.org/10.1038/s41550-023-02103-9)
- van Dokkum, P. G., Franx, M., Kriek, M., et al. 2008, ApJL, 677, L5, doi: [10.1086/587874](https://doi.org/10.1086/587874)
- van Dokkum, P. G., Nelson, E. J., Franx, M., et al. 2015, ApJ, 813, 23, doi: [10.1088/0004-637X/813/1/23](https://doi.org/10.1088/0004-637X/813/1/23)
- Veilleux, S., Cecil, G., & Bland-Hawthorn, J. 2005, ARA&A, 43, 769, doi: [10.1146/annurev.astro.43.072103.150610](https://doi.org/10.1146/annurev.astro.43.072103.150610)
- Vesperini, E., & Heggie, D. C. 1997, MNRAS, 289, 898, doi: [10.1093/mnras/289.4.898](https://doi.org/10.1093/mnras/289.4.898)
- Wang, B., Heckman, T. M., Zhu, G., & Norman, C. A. 2020, ApJ, 894, 149, doi: [10.3847/1538-4357/ab88b4](https://doi.org/10.3847/1538-4357/ab88b4)
- Wang, B., Leja, J., Bezanson, R., et al. 2023, ApJL, 944, L58, doi: [10.3847/2041-8213/acba99](https://doi.org/10.3847/2041-8213/acba99)
- Wang, B., de Graaff, A., Davies, R. L., et al. 2024a, arXiv e-prints, arXiv:2403.02304, doi: [10.48550/arXiv.2403.02304](https://doi.org/10.48550/arXiv.2403.02304)
- Wang, B., Leja, J., Labbé, I., et al. 2024b, ApJS, 270, 12, doi: [10.3847/1538-4365/ad0846](https://doi.org/10.3847/1538-4365/ad0846)
- Wang, B., Leja, J., Atek, H., et al. 2024c, ApJ, 963, 74, doi: [10.3847/1538-4357/ad187c](https://doi.org/10.3847/1538-4357/ad187c)

- Weibel, A., Oesch, P. A., Barrufet, L., et al. 2024, arXiv e-prints, arXiv:2403.08872, doi: [10.48550/arXiv.2403.08872](https://doi.org/10.48550/arXiv.2403.08872)
- Weiner, B. J., Willmer, C. N. A., Faber, S. M., et al. 2006, ApJ, 653, 1027, doi: [10.1086/508921](https://doi.org/10.1086/508921)
- Wellons, S., Torrey, P., Ma, C.-P., et al. 2015, MNRAS, 449, 361, doi: [10.1093/mnras/stv303](https://doi.org/10.1093/mnras/stv303)
- Williams, C. C., Alberts, S., Ji, Z., et al. 2023, arXiv e-prints, arXiv:2311.07483, doi: [10.48550/arXiv.2311.07483](https://doi.org/10.48550/arXiv.2311.07483)
- Worthey, G., Faber, S. M., Gonzalez, J. J., & Burstein, D. 1994, ApJS, 94, 687, doi: [10.1086/192087](https://doi.org/10.1086/192087)
- Wuyts, S., Förster Schreiber, N. M., Wisnioski, E., et al. 2016, ApJ, 831, 149, doi: [10.3847/0004-637X/831/2/149](https://doi.org/10.3847/0004-637X/831/2/149)
- Yue, M., Eilers, A.-C., Annana, T. T., et al. 2024, arXiv e-prints, arXiv:2404.13290, doi: [10.48550/arXiv.2404.13290](https://doi.org/10.48550/arXiv.2404.13290)